13 Feb 2024

CO2 Uptake By Microporous Carbon Aerogels Derived From Polybenzoxazine And Analogous All-Nitrogen Polybenzodiazine Aerogels

Vaibhav A. Edlabadkar

Rushi U. Soni

A. B.M.Shaheen ud Doulah

Stephen Y. Owusu

et. al. For a complete list of authors, see https://scholarsmine.mst.edu/chem_facwork/3678

Recommended Citation

V. A. Edlabadkar et al., "CO2 Uptake By Microporous Carbon Aerogels Derived From Polybenzoxazine And Analogous All-Nitrogen Polybenzodiazine Aerogels," *Chemistry of Materials*, vol. 36, no. 3, pp. 1172 - 1187, American Chemical Society, Feb 2024.
The definitive version is available at https://doi.org/10.1021/acs.chemmater.3c01717

CHEMISTRY OF MATERIALS

pubs.acs.org/cm

Article

CO_2 Uptake by Microporous Carbon Aerogels Derived from Polybenzoxazine and Analogous All-Nitrogen Polybenzodiazine Aerogels

Vaibhav A. Edlabadkar, Rushi U. Soni, A. B. M. Shaheen ud Doulah, Stephen Y. Owusu, Samuel Hackett, Joshua M. Bartels, Nicholas Leventis,* and Chariklia Sotiriou-Leventis*

Cite This: *Chem. Mater.* 2024, 36, 1172−1187

Read Online

ACCESS | Metrics & More | Article Recommendations | Supporting Information

ABSTRACT: The rapid rise of carbon dioxide in the atmosphere contributes to global warming and ocean acidification. Carbon capture is considered essential for keeping the atmospheric CO_2 levels from rising further. This work addresses the question of whether nitrogen or oxygen lining of the surfaces of carbon-based CO_2 absorbers is more efficient for CO_2 capture. Polybenzodiazine (PBDAZ) aerogels are carbon-aerogel precursors that were prepared recently (2023) as all-nitrogen structural analogues to well-known polybenzoxazine (PBO) aerogels. However, owing to the fact that the carbonization chemistries of both PBO and PBDAZ aerogels require a prior oxidative aromatization step in air at around 200−240 °C, both types of the resulting carbon (C) aerogels contained both oxygen and nitrogen in their structures. As a carryover from their polymeric aerogel precursors, C-PBDAZ aerogels included a higher weight percent of N (7−11%) relative to the C-PBO aerogels (5.2−5.7%) while both types of carbons included about the same amount of O (7−9%). Activation (etching) with CO_2 at 1000 °C removed more N than O, so the resulting etched carbon aerogels from either source (EC-PBDAZ or EC-PBO) contained about 8−9% of O and only 3.0−3.6% N. Postetching, most oxygen was situated in pyridonic and nitroxide sites (by XPS). Looking at the PBDAZ- and PBO-derived C and EC aerogels independently, whenever processing increased the O/N ratio within each material, the CO_2 uptake (at 273 K, 1 bar) also increased, reaching 11.5 mmol g^{-1} in EC-PBDAZ and 4.6 mmol g^{-1} in EC-PBO aerogels, starting from 7.0 mmol g^{-1} by C-PBDAZ and 3.0 mmol g^{-1} by C-PBO. Subsequently, by eliminating the relative pore volumes and surface areas as causing the different CO_2 uptakes by the two types of materials, the highest CO_2 uptake by the EC-PBDAZ aerogels was attributed to the pore sizes (diameters in the 3−4 nm range) in combination with the geometry of the CO_2-surface adducts. EC-PBDAZ carbon aerogels showed high selectivity for CO_2 versus H_2 (up to 404:1—relevant to precombustion CO_2 capture) and high selectivity for CO_2 versus N_2 (up to 48:1—relevant to postcombustion CO_2 capture).

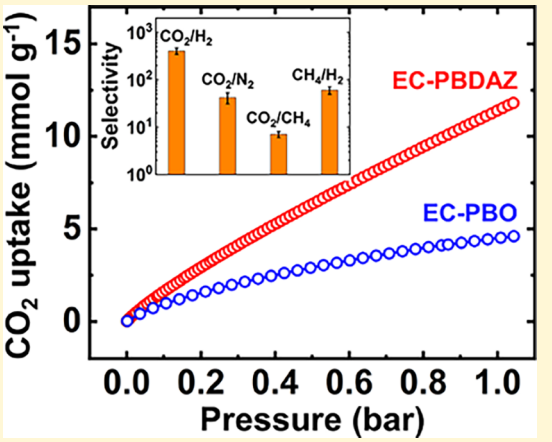

1. INTRODUCTION

Over the last 200 years, the atmospheric concentration of greenhouse gases has doubled.[1] Specifically, that of CO_2 has increased from a preindustrial level of 280 ppm to over 420 ppm in 2023.[2] Over the same period, the average global temperature has increased by 1.5 °C.[3] The link between accumulation of greenhouse gases in the atmosphere and global warming leaves practically no doubt that the climate change is anthropogenic and traceable directly to the use and burning of fossil fuels.[4−6] The global CO_2 emissions saw a significant reduction in the economic slowdown of the 2020−2022 period,[7] but pandemics cannot be the solution to climate change! Instead, carbon capture and sequestration (CCS) have been considered a viable approach to reduce the release of CO_2 in the atmosphere. CCS aims at intercepting CO_2 emissions at the point of their large-scale generation, like power plants, followed by permanent storage in ways that will not allow return to the atmosphere.[8,9]

To date, three main technologies have been used to separate CO_2 from industrial emission sources: use of scrubbing solutions,[10] use of solid sorbents,[11] and membranes.[12] Solid sorbents have several advantages when it comes to transportation, possible recovery, or permanent disposal and include metal−organic frameworks (MOF),[13,14] hyper-cross-

Received: July 9, 2023
Revised: November 17, 2023
Accepted: November 20, 2023
Published: January 18, 2024

https://doi.org/10.1021/acs.chemmater.3c01717
Chem. Mater. 2024, 36, 1172−1187

linked polymers (HCP),[15] conjugated microporous polymers (CMPs),[16] polymers with intrinsic microporosity (PIMs),[17] porous aromatic frameworks (PAF),[18] microporous organic polymers (MOPs),[19] porous polymer frameworks (PPFs),[20] benzimidazole-linked polymers (BILP).[21] Notwithstanding the relative costs, some of these approaches have inherent materials issues, for example sensitivity to moisture, like most of MOFs.[22,23] However, the most general issue with the majority of these materials is that they are obtained as powders and therefore must be repackaged in form factors that will allow nearly unobstructed flow of gases through their bulk, yet they will still provide enough contact time for gas uptake.[24−26] Those requirements are akin to the function of multilevel devices like catalytic converters.[27−29] Then, a reasonable value proposition for efficient CO_2 capture by solid sorbents is to concentrate many of the functions of catalytic converters into a single material with a hierarchical porous structure. In that regard, aerogels are a class of multiscale nanoporous materials offering almost unobstructed gas diffusion through their bulk,[30] and may foot the bill.

Among aerogels, those based on carbon are especially attractive because they are chemically inert, are physicochemically stable, display wide multiscale pore size distributions, and have high surface areas.[31] Carbon aerogels come from the pyrolysis of suitable polymeric aerogels, which in turn are synthesized using typical sol−gel chemistry. Chemical transformations during pyrolytic carbonization are responsible for the rigidity[32−34] and the high porosity of carbon aerogels.[35]

Many classes of polymeric aerogels may yield carbon aerogels, for example aromatic polyamides,[27] polyimides,[36,37] polyurethanes,[38] and polyureas.[39,40] However, most carbon aerogels come from phenolic-resin type of polymeric aerogels like those from condensation of resorcinol formaldehyde (RF),[33,41−43] phenol formaldehyde, phloroglucinol formaldehyde, and phloroglucinol−terepthaldehyde[33] and like those from ring opening of suitable monomers like polybenzoxazine aerogels (PBOs)[34,44] and more recently polybenzodiazine (PBDAZ) aerogels.[45]

Motivated by the capture of CO_2 by solutions of amines,[10] it has been proposed that a way to improve CO_2 absorption is by incorporating nitrogen into the carbon framework.[46,47] However, the role of nitrogen heteroatoms in CO_2 absorption by carbon aerogels has been debated, as among the best absorbers in this class of materials are carbon aerogels that do not contain any nitrogen at all.[48] Instead, oxygen heteroatoms lining the surfaces of micropores and small mesopores in the mesopore−micropore borderline seem to be quite effective for reversible uptake of significant amounts of CO_2.

In this work, we studied the role of oxygen versus nitrogen heteroatoms in the CO_2 uptake capacity of carbon aerogels by comparing the behavior of carbon aerogels coming from PBDAZ[45] and from PBO aerogels.[34] As shown in Scheme 1, PBDAZ contains only nitrogen while PBO contains both N and O. Owing to the structural similarity of PBDAZ and PBO aerogels, their pyrolytic chemistry is identical: for quantitative carbonization, both types of aerogels need to undergo complete oxidative ring-fusion aromatization, which is carried out under O_2 or air at relatively low temperatures (200−240 °C). Aromatized PBDAZ and PBO aerogels (refer to Scheme 1) were carbonized in high yields at 600 and 800 °C under Ar. The microporosity of both types of carbon aerogels received after pyrolysis at either temperature increased by reactive etching with CO_2 at 1000 °C. Carbon and etched carbon

Scheme 1. Monomers, PBO, and PBDAZ Polymers and Their Oxidized Forms

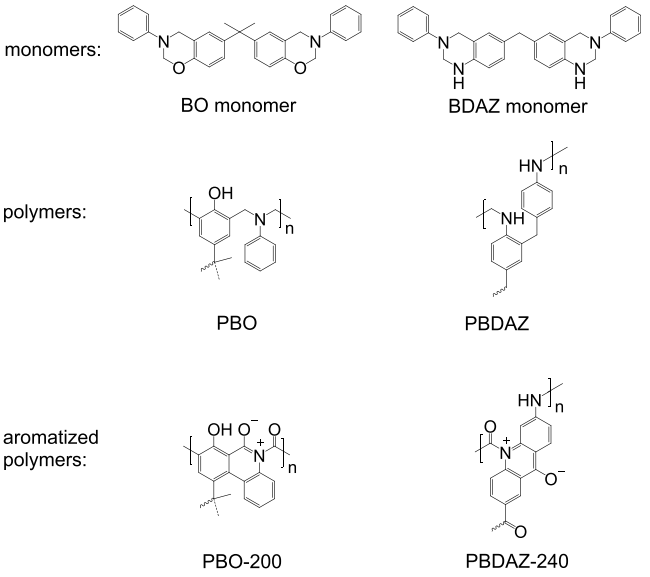

aerogels derived from PBDAZ and PBO were evaluated for their CO_2 absorption capacities. The highest CO_2 uptake (in the range of 11−12 mmol g^{-1} at 273 K/1 bar) was obtained from highly microporous etched carbon aerogels derived from PBDAZ aerogels. In fact, these values were higher than those reported for most porous carbon-based CO_2 sorbents we are aware of, except from certain carbonized and CO_2-etched RF aerogels.[48] By comparison, analogous highly microporous etched carbon aerogels from PBO aerogels absorbed much less CO_2 under the same conditions (in the range of only 4−5 mmol g^{-1}). At first glance, these results seem to support the nitrogen hypothesis; however, owing to the oxidation and later the etching step, carbon and especially etched carbon aerogels from both PBDAZ and PBO aerogels contain comparable amounts of oxygen, higher than nitrogen, situated in chemically similar functionalities for binding with CO_2 (e.g., $-O^-$). The higher CO_2 uptake by carbon aerogels derived from PBDAZ was attributed to the relative size of micropores.

2. RESULTS AND DISCUSSION

2.1. Preparation of Carbon and Etched Carbon Aerogels from PBDAZ and PBO. The monomer precursors of PBO and PBDAZ aerogels were prepared via different routes.[34,45] However, owing to the structural similarity of the two monomers (Scheme 1), subsequent chemical transformations during gelation and further processing of the derived aerogels were quite similar (Scheme 2). In both cases, HCl-catalyzed ring-opening polymerization of the monomers was carried out in DMF. PBDAZ wet gels were obtained at 100 °C, while PBO gels were obtained at room temperature. The gelation solvent was exchanged with acetone, and wet gels were dried into aerogels with liquid CO_2 that was converted to a supercritical fluid (SCF) and vented off like a gas. As-prepared aerogels are referred to by the abbreviations of the respective polymers (PBDAZ and PBO). Reflecting the common ring-opening polymerization chemistry, PBO and PBDAZ aerogels were structurally similar; however, the former contains both oxygen and nitrogen heteroatoms while PBDAZ contains only nitrogen (Scheme 1). Reasoning by analogy to the pyrolytic chemistry of polyacrylonitrile,[49,50] it was discovered that for

https://doi.org/10.1021/acs.chemmater.3c01717
Chem. Mater. 2024, 36, 1172−1187

Scheme 2. Preparation and Pyrolytic Processing of PBDAZ and PBO Aerogels

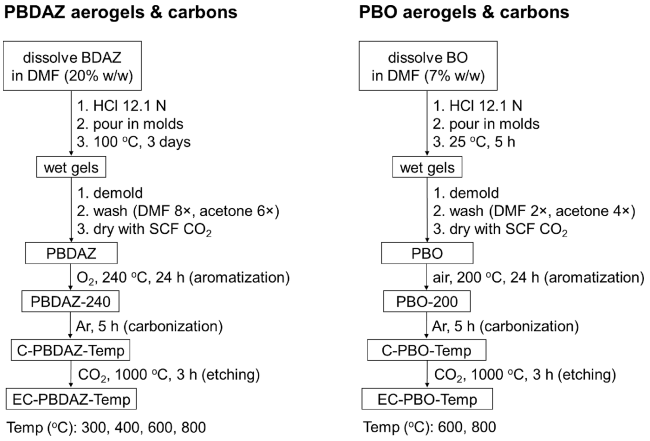

quantitative carbonization, both PBO and PBDAZ should be subjected to an oxidative ring-fusion aromatization step at relatively low temperatures under oxygen or air.[34,45] The resulting materials are termed PBDAZ-240 and PBO-200, where the numerical extensions refer to the oxidation/aromatization temperatures. The prevalent structures of the oxidized forms are included in Scheme 1. It is noted that post oxidation/aromatization, both PBDAZ-240 and PBO-200 include nitrogen and oxygen heteroatoms. However, as a carryover from the parent polymer, PBDAZ-240 contains more nitrogen per oxygen atom than PBO-200. Further pyrolysis of the oxidized/aromatized samples was conducted under Ar. PBDAZ-240 aerogels were pyrolyzed at Temp = 300, 400, 600, and 800 °C, while PBO-200 aerogels were pyrolyzed at Temp = 600 and 800 °C (Scheme 2). The resulting aerogels are referred to as C-PBDAZ-Temp and C-PBO-Temp, respectively. Finally, C-PBDAZ-Temp and C-PBO-Temp aerogels were subjected to reactive etching at 1000 °C under flowing CO_2 (Scheme 2) and the resulting etched-carbon aerogels are termed EC-PDBAZ-Temp and EC-PBO-Temp, respectively.

2.2. The Evolution of the General Material Properties, the Skeletal Framework, and the Porous Structure along Processing. *2.2.a. General Material Properties.* General material properties during processing (Scheme 2) are summarized in Table 1. As-prepared PBDAZ aerogels shrank less (25 ± 2%) than their PBO counterparts (33 ± 0.3%). By the end of the ring-fusion aromatization process, both PBDAZ-240 and PBO-200 had shrunk about the same extent relative to the molds (36 and 38%, respectively). Further pyrolysis of PBDAZ-240 up to 400 °C did not cause any additional shrinkage. An additional 7−10% shrinkage was introduced into the PBDAZ-240 aerogels by pyrolysis at 600 and 800 °C, ending up at 42 and 47%, respectively, relative to the molds. The shrinkage of C-PBO-600 and C-PBO-800 aerogels was similar (45 and 50%, respectively). The linear shrinkage of all etched EC-PBDAZ-Temp samples was practically the same, which is around 47−48% relative to the molds, irrespective of the initial Temp (pyrolysis temperature). EC-PBO-Temp aerogels shrunk 52−54% after etching.

Although the BDAZ monomer concentration was 3× higher than the concentration of the BO monomer in the respective sols, mass loss of soluble oligomers during postgelation washes caused the bulk density (ρ_b) of as-prepared PBDAZ aerogels to be lower (0.195 g cm^{-3}) than of the corresponding PBO (0.244 g cm^{-3})—see Table 1. This difference in bulk densities was maintained after ring-fusion aromatization (PBDAZ-240: 0.236 g cm^{-3} versus PBO-200: 0.287 g cm^{-3}). Reflecting the differential shrinkage and the mass loss upon further pyrolysis, the ρ_b values of C-PBDAZ-Temp remained in the range of 0.22−0.26 g cm^{-3}. The bulk densities of C-PBO-600 and C-PBO-800 were also in the same range: 0.23 and 0.30 g cm^{-3}, respectively. Etching caused significant mass losses in both series of samples. The yields of EC-PBDAZ-Temp and EC-

Table 1. Material Properties of PBDAZ- and PBO-Derived Carbon and Etched Carbon Aerogels

					specific pore volume [cm^3 g^{-1}]				average pore diameter [nm] via $4 \times V/\sigma$[i]	
sample	linear shrinkage [%][a,b]	bulk density, ρ_b [g cm^{-3}][a]	skeletal density, ρ_s [g cm^{-3}][c]	porosity Π [% v/v][d]	V_{Total}[e]	V_{max}[f]	$V_{1.7-300\_nm}$[g]	surface area BET, σ (micropore)[h] [m^2 g^{-1}]	$V = V_{Total}$	$V = V_{max}$
PBDAZ	$25._1 \pm 2.0$	0.195 ± 0.008	1.575 ± 0.003	88	4.50	0.03	0.03	18 (3)	998	6.6
PBO	32.9 ± 0.3	0.244 ± 0.001	1.320 ± 0.007	82	3.34	0.14	0.12	60 (0)	223	9.3
PBDAZ-240	$35._7 \pm 0.07$	0.236 ± 0.005	1.442 ± 0.009	84	3.54	0.10	0.03	42 (4)	338	9.5
PBO-200	37.5 ± 0.9	0.287 ± 0.005	1.533 ± 0.051	81	2.83	0.10	0.08	55 (2)	206	7.3
C-PBDAZ-300	36.2 ± 0.3	0.258 ± 0.005	1.579 ± 0.014	83	3.24	0.05	0.04	23 (3)	563	8.7
C-PBDAZ-400	37.6 ± 0.2	0.231 ± 0.002	1.637 ± 0.006	86	3.71	0.07	0.05	37 (8)	402	7.6
C-PBDAZ-600	42.4 ± 0.2	0.216 ± 0.005	1.941 ± 0.03	89	4.11	0.27	0.06	432 (342)	38	2.5
C-PBDAZ-800	46.8 ± 0.1	0.225 ± 0.001	2.197 ± 0.018	90	3.99	0.19	0.05	346 (274)	46	3.0
C-PBO-600	44.8 ± 0.1	0.217 ± 0.001	1.879 ± 0.014	88	4.08	0.36	0.13	472 (334)	35	2.9
C-PBO-800	50.2 ± 0.3	0.303 ± 0.004	1.987 ± 0.030	85	2.70	0.29	0.12	351 (252)	22	3.3
EC-PBDAZ-300	47.1 ± 0.3	0.129 ± 0.003	2.288 ± 0.034	94	7.31	1.07	0.17	1818 (1273)	16	2.4
EC-PBDAZ-400	47.9 ± 0.2	0.123 ± 0.006	2.269 ± 0.021	94	7.68	1.15	0.18	2121 (1234)	14	2.2
EC-PBDAZ-600	47.6 ± 0.1	0.132 ± 0.003	2.238 ± 0.016	94	7.12	1.10	0.18	1913 (1232)	15	2.3
EC-PBDAZ-800	47.5 ± 0.6	0.152 ± 0.012	2.184 ± 0.012	93	6.12	1.02	0.21	1650 (950)	15	2.4
EC-PBO-600	52.2 ± 0.2	0.119 ± 0.028	1.983 ± 0.060	94	7.90	1.23	0.34	1850 (1030)	17	2.6
EC-PBO-800	54.0 ± 0.3	0.179 ± 0.013	1.953 ± 0.011	91	6.75	1.11	0.35	1591 (1038)	17	2.8

[a]Average of five samples. [b]All values relative to the molds. [c]Single sample, average of 50 measurements. [d]Via $\Pi = 100 \times (\rho_s - \rho_b)/\rho_s$. [e]$V_{Total} = (1/\rho_b) - (1/\rho_s)$. [f]$V_{max}$: single-point N_2 adsorption at 77 K as $P/P_0 \rightarrow 1.0$. [g]BJH-desorption cumulative pore volume. [h]Via the *t*-plot method. [i]For V_{Total} and V_{max} refer to footnotes (e) and (f).

https://doi.org/10.1021/acs.chemmater.3c01717
Chem. Mater. 2024, 36, 1172−1187

PBO-Temp aerogels were calculated from their respective aromatized versions, PBDAZ-240 and PBO-200, and were in the ranges 21−22 and 17−20%, respectively. Combination of these slightly higher yields of EC-PBDAZ-Temp and slightly lower shrinkages relative to EC-PBO-Temp brought the bulk densities of all EC-PBDAZ-Temp aerogels (0.12−0.15 g cm^{-3}) in the same range as the densities of EC-PBO-600 and EC-PBO-800 (0.12 and 0.18 g cm^{-3}, respectively).

The skeletal densities (ρ_s) of C-PBDAZ-Temp aerogels increased steadily with the pyrolysis temperature from 1.6 g cm^{-3} (C-PBDAZ-300) to 2.2 g cm^{-3} (C-PBDAZ-800). Postetching, the ρ_s values of all EC-PBDAZ-Temp were in the 2.2−2.3 g cm^{-3} range. This evolution of the ρ_s values with the pyrolysis temperature suggested the presence of closed that became accessible partly after pyrolysis at 800 °C and mainly by reactive etching with CO_2. A somewhat similar trend was noted with C- and EC-PBO-600_or_800 aerogels: after etching, the ρ_s value of C-PBO-800 (2.0 g cm^{-3}) remained the same while the ρ_s value of C-PBO-600 (1.9 g cm^{-3}) increased to 2.0 g cm^{-3} presumably by rendering accessible a small amount of closed micropores. Open porosities, Π, were calculated from the ρ_s and ρ_s values via $\Pi = 100 \times (\rho_s - \rho_b)/\rho_s$. Π values for both C-PBDAZ-Temp and C-PBO-Temp aerogels were in the range of 83−90% v/v and reached up to 94% v/v after reactive etching with CO_2 at 1000 °C.

2.2.b. The Skeletal Framework. Microscopically, all C-PBDAZ-Temp, C-PBO-Temp, EC-PBDAZ-Temp, and EC-PBO-Temp aerogels consisted of nanoparticles fused together to secondary aggregates, which, in turn, assembled randomly to form larger structures that included large, interconnected voids (macropores) perforating the entire bulk (Figure 1A,B).

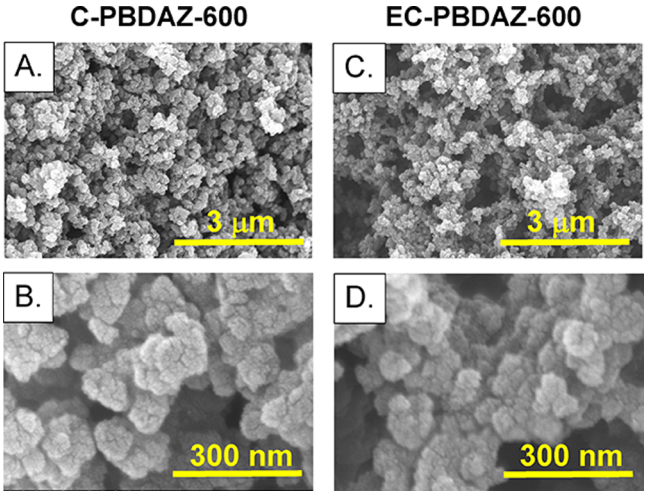

Figure 1. Representative SEM images at two different magnifications of C-PBDAZ-600 aerogels (left) and the same aerogels after reactive etching with CO_2 (EC-PBDAZ-600, right). (A) C-PBDAZ-600. (B) C-PBDAZ-600 at higher magnification. (C) EC-PBDAZ-600. (D) EC-PBDAZ-600 at higher magnification.

Consistent with the shrinkage data (Table 1), after etching, the higher-level structures were preserved (Figure 1C), and interestingly the smallest discernible nanoparticles along the skeletal framework became better defined (Figure 1D). These SEM features were present in all pyrolysis products from both PBDAZ and PBO. The porous network was probed quantitatively with medium-pressure N_2-sorption porosimetry at 77 K. The microporosity formed by the smallest skeletal nanoparticles (not visible in SEM) was probed with low-pressure N_2-sorption porosimetry at 77 K.

2.2.c. The Meso- and Macroporosity. N_2-sorption isotherms of all postoxidation pyrolytic materials are shown in Figure 2. Data derived from these isotherms are summarized in

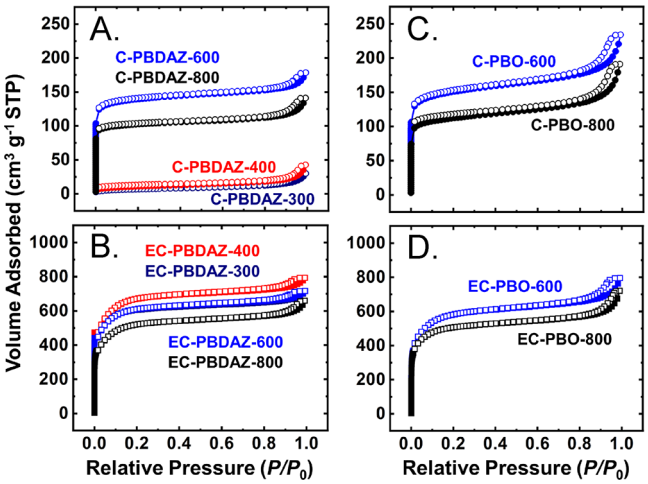

Figure 2. N_2-sorption isotherms at 77K of all carbonized (top row) and etched carbon aerogels (lower row) of all PBDAZ-derived (A, B) and PBO-derived (C, D) aerogels (color coding and sequence of labels inside the frames follow the sequence of the corresponding isotherms.).

Table 1. For cross-referencing purposes, Table 1 also includes data derived from the N_2 sorption isotherms of as-prepared and of the aromatized versions of PBDAZ and PBO.[34,45] The isotherms of C-PBDAZ-300 and -400 aerogels showed very low volumes of adsorbed N_2 (<50 cm^3 g^{-1}, Figure 2A). The isotherms of samples pyrolyzed at 600 and 800 °C, namely, C-PBDAZ-600_or_800 and C-PBO-600_or_800, showed rapid rises at $P/P_0 \ll 0.1$ into the 100−200 cm^3 g^{-1} range, pointing at the creation of microporosity (pores with sizes less than 2 nm) at those pyrolytic temperatures, in line with conclusions from skeletal density data. Typically, simple pyrolysis of carbonizable polymeric aerogels does not create microporosity; it is speculated that the microporosity of just-pyrolyzed samples here is the result of the rigidization imposed by the oxidative ring-fusion aromatization step.[34,45] At the same time, the hysteresis loops of the same samples at $P/P_0 > 0.9$ were small, indicating only a small amount of mesoporosity. To quantify this conjecture, the specific total pore volumes of all materials were calculated via $V_{Total} = (1/\rho_b) - (1/\rho_s)$ and were compared with V_{max}, which is the total specific volume of N_2 uptaken by each sample at the maximum point of its N_2-sorption isotherm, i.e., as $P/P_0 \rightarrow 1$. The mesoporous fraction of V_{max}, referred to as $V_{1.7-300\_nm}$, was obtained from the desorption branch of the isotherms at $P/P_0 \rightarrow 1$ using the BJH method. V_{Total}, V_{max}, and $V_{1.7-300\_nm}$ are included in Table 1. For all C-type materials, V_{Total} was always much larger than V_{max} (up to 60×) consistent with the macroporosity noted in SEM. In turn, V_{max} was about equal to $V_{1.7-300\_nm}$ only in C-PBDAZ-300 and C-PBDAZ-400, while in C-PBDAZ-600_or_800 and C-PBO-600_or_800, $V_{max} \approx 2.5-5.5 \times V_{1.7-300\_nm}$, consistent with the appearance of microporosity as concluded above qualitatively based on the shape of the isotherms at $P/P_0 \ll 0.1$. In fact, as it emerges from this discussion, an estimate of $V_{micropore}$ can be obtained from these

https://doi.org/10.1021/acs.chemmater.3c01717
Chem. Mater. 2024, 36, 1172−1187

Table 2. Micropore Analysis and CO_2 Uptake Data by PBDAZ- and PBO-Derived Carbon and Etched Carbon Aerogels

	specific "micropore" volume, $V_{micropore}$ [$cm^3\ g^{-1}$]					micropore diameter [nm] via 4× $V_{micropore}$/(micropore area)[f]		CO_2 uptake [mmol g^{-1}] at 273 K, 1 bar				
									calculated from			
									surface areas[g]		$V_{micropore}$	
sample	from data in Table 1[a]	via $DR(N_2)$[b]	via $HK(N_2)$[c]	via $DR(CO_2)$[d]	via $DFT(CO_2)$[e]	$V_{micropore}$ from $DR(N_2)$[b]	$V_{micropore}$ from $DR(CO_2)$[d]	measured	BET	micro	$DR(N_2)$[h]	Q_0 [kJ mol^{-1}][i]
C-PBDAZ-300	0.01			0.19 ± 0.02	0.04 ± 0.00		1.9	2.68 ± 0.3	0.39	0.07		21
C-PBDAZ-400	0.02			0.36 ± 0.08	0.07 ± 0.01		1.9	5.05 ± 0.1	0.36	0.08		23
C-PBDAZ-600	0.21	0.20	0.19	0.50 ± 0.03	0.13 ± 0.03	2.3	5.5	6.95 ± 0.2	4.21	3.34	4.65	23
C-PBDAZ-800	0.14	0.16	0.15	0.36 ± 0.09	0.10 ± 0.01	2.5	4.7	5.51 ± 0.1	3.02	2.48	3.71	19
C-PBO-600	0.23	0.21	0.19	0.22 ± 0.02	0.05 ± 0.00	2.5	2.6	2.97 ± 0.2	4.21	2.67	4.88	19
C-PBO-800	0.17	0.20	0.18	0.19 ± 0.02	0.06 ± 0.00	2.0	2.2	2.80 ± 0.1	3.42	2.46	4.65	19
EC-PBDAZ-300	0.90	1.16	0.93	1.13 ± 0.19	0.16 ± 0.02	3.6	3.6	11.50 ± 0.8	17.75	12.43	26.97	36
EC-PBDAZ-400	0.97	1.31	1.05	1.00 ± 0.05	0.14 ± 0.00	4.2	3.2	11.27 ± 0.4	20.71	12.05	30.45	25
EC-PBDAZ-600	0.92	1.13	0.57	0.96 ± 0.09	0.13 ± 0.00	3.6	3.1	10.97 ± 1.0	18.68	12.03	26.27	28
EC-PBDAZ-800	0.81	0.98	0.54	0.85 ± 0.05	0.14 ± 0.02	4.1	3.6	10.20 ± 0.9	16.11	9.27	22.66	34
EC-PBO-600	0.89	0.71	0.57	0.42 ± 0.01	0.11 ± 0.00	2.8	1.6	4.35 ± 0.1	18.06	10.05	16.50	15
EC-PBO-800	0.76	0.70	0.55	0.39 ± 0.03	0.12 ± 0.00	2.7	1.5	4.60 ± 0.2	15.53	10.13	16.27	19

[a] $V_{micropore} = V_{max} - V_{1.7-300\_nm}$ using data from Table 1. [b] Via the Dubinin–Radushkevich (DR) method,[52] from N_2-sorption data obtained at 77 K using a low-pressure transducer ($P/P_0 \leq 0.01$). [c] Via the Horvath–Kawazoe (HK) method,[53] using the same low-pressure N_2-sorption data used in the DR method. [d] Via the DR method using CO_2 adsorption data at 273 K up to a relative pressure of 0.03 (1 atm). Data are averages from three experiments. [e] As in footnote (d) using the DFT method. The pore volumes reported concern pores <1 nm in size. [f] Calculated using micropore surface areas via the *t*-plot method (refer to Table 1). [g] Calculated by dividing the BET surface area (left column), or the micropore surface area (right column) by the CO_2 cross sectional area (0.17 nm^2) and Avogadro's number. [h] By assuming that the micropore volume calculated via the $DR(N_2)$ method (footnote b) was filled with liquid CO_2. The density of liquid CO_2 at 273 K was set equal to the density of the uptaken CO_2 (1.023 g cm^{-3}).[54] [i] Heat of CO_2 adsorption at zero coverage calculated using virial fitting of the CO_2 isotherms at two different temperatures (see Section 4.2).

medium-pressure N_2-sorption data via $V_{micropore} = V_{max} - V_{1.7-300\_nm}$ and these values may be used to crosscheck micropore volumes calculated from the low-pressure parts of the N_2-sorption isotherms of Figure 2 (see Section 2.2.d below).

After etching with CO_2 at 1000 °C, the V_{Total} of all EC-PBDAZ-Temp and EC-PBO-Temp aerogels, irrespective of the Temp, almost doubled (Table 1). Simultaneously, the volumes of N_2 adsorbed at $P/P_0 \ll 0.1$ also increased dramatically (by 5–6×) while no significant change could be seen on the high-pressure loops as $P/P_0 \rightarrow 1$ (Figure 2). Quantitatively, both V_{max} and $V_{1.7-300\_nm}$ increased but V_{max} increased more, reflecting the increase in microporosity as implied by the isotherms. These data, in combination with the skeletal density and SEM data, confirmed that the skeletal frameworks of just-carbonized materials included significant amounts of closed microporosity that became accessible by reactive etching. In particular, the better definition of primary particles in postetching SEM (Figure 1D) suggests that the "glazing" observed over the skeletal framework in pre-etching SEM images (Figure 1B) is what blocked access to the micropores and rendered them closed.

BET surface areas, σ, were calculated from medium-pressure N_2-sorption data. Micropore areas were calculated via *t*-plot analysis with the Harkins and Jura (HK) method.[51] All data are listed in Table 1. The surface areas of all as-prepared, aromatized, and subsequently pyrolyzed at Temp ≤400 °C samples were lower than 60 $m^2\ g^{-1}$. Samples first aromatized (PBDAZ-240 and PBO-200) and subsequently pyrolyzed at 600 and 800 °C displayed BET surface areas in the 346–472 $m^2\ g^{-1}$ range, with 71% of those values in C-PBO-Temp and 80% of those values in C-PBDAZ-Temp allocated to micropores (Temp = 600 and 800 °C). Irrespective of Temp, reactive etching under CO_2 at 1000 °C of all C-PBDAZ-Temp and C-PBO-Temp resulted in a dramatic increase in the BET surface areas reaching values as high as 2121 $m^2\ g^{-1}$ (case of EC-PBDAZ-400). Of those surface areas, on average, 55–64% was allocated to micropores. If the objective is microporous carbons, prior carbonization under inert atmosphere (Ar) can be bypassed by taking freshly aromatized materials directly to 1000 °C under CO_2.

Finally, the average pore diameters were calculated via the $4V/\sigma$ method. Two independent sets of pore volumes, *V*, were used for that calculation: one by setting $V = V_{Total}$ and a second one by setting $V = V_{max}$. The pore diameters calculated via the two methods diverged from one another for all of the materials (Table 1). Pore diameters obtained by setting $V = V_{Total}$ were significantly larger than those calculated by setting $V = V_{max}$, which reflects the fact that all porosities were essentially bimodal, consisting of large macropores (refer to the SEM) and micropores (refer to the N_2 sorption isotherms). Interestingly, irrespective of the temperature of the initial pyrolysis of the aromatized samples, Temp, the pore diameters calculated for both EC-PBDAZ-Temp and EC-PBO-Temp aerogels via $V = V_{Total}$ or $V = V_{max}$ remained all within the ranges of 14–17 nm and 2.2–2.8 nm, respectively, underlining the fact that postreactive etching the structures of all carbon aerogels converged.

2.2.d. Microporosity. Specific micropore volumes, $V_{micropore}$, and micropore sizes are both relevant to CO_2 absorption and were calculated by using three independent methods. Results are summarized in Table 2. The first method was based on medium-pressure N_2-sorption data (P/P_0 >0.1, Figure 2 and Table 1) and utilized $V_{1.7\text{-}to\text{-}300\_nm}$ and V_{max}. (As mentioned in the previous section, V_{max} is the sum of $V_{micropore}$ and $V_{1.7\text{-}to\text{-}300\_nm}$ and therefore $V_{micropore} = V_{max} - V_{1.7\text{-}to\text{-}300\_nm}$.) The upper cutoff limit of this method is at 1.7 nm, and thus, it may not account for small pores above 1.7 nm, which can still

https://doi.org/10.1021/acs.chemmater.3c01717
Chem. Mater. 2024, 36, 1172–1187

be relevant to CO_2 adsorption. As it turns out, this is the case here. Nevertheless, these $V_{micropore}$ values serve as a cross check for the validity of the micropore volume calculation via the second method, which is based on the low-pressure (LP) N_2-sorption data at 77 K, namely, on the rapidly rising branch of the isotherms of Figure 2 at $P/P_0 \ll 0.1$. Specific micropore volumes were calculated from these data by applying either the Dubinin–Radushkevich (DR),[52] or the Horvath–Kawazoe (HK)[53] method of analysis. In general, there was good agreement between the first (medium-pressure N_2-sorption method) and the low-pressure N_2-sorption results via the DR(N_2) method. The HK(N_2) method gave lower pore volumes than the DR(N_2) method and even lower values than the medium-presume N_2-sorption method for all EC samples that had been carbonized at 600 and 800 °C. Thereby, micropore volumes via the HK(N_2) method were deemed questionable and were not considered further. The third method for calculating $V_{micropore}$ was based on the CO_2 adsorption data at 0 °C up to a pressure of 1 bar (Figure 3).

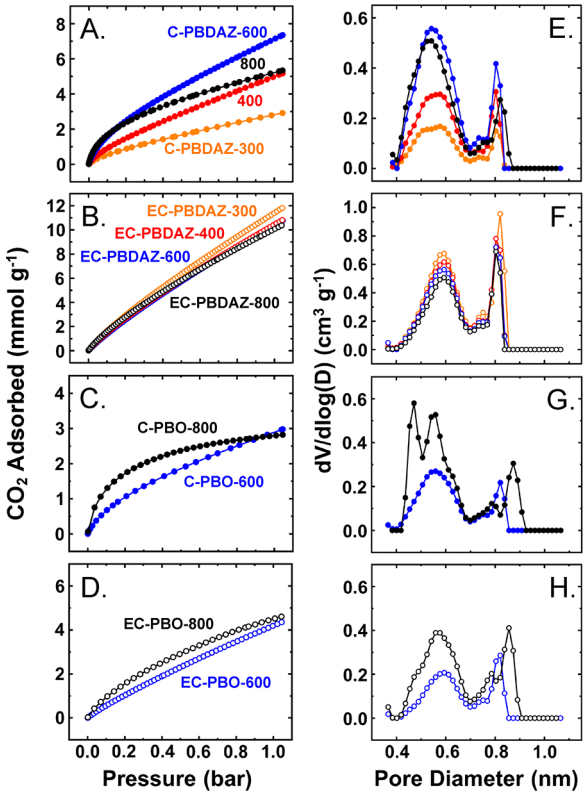

Figure 3. CO_2 adsorption isotherms (left) and pore size distributions using the DFT method (right) of carbon (C-) and etched carbon (EC-) aerogels. (A, E) As-prepared C-PBDAZ-Temp aerogels. (B, F) Carbonized and etched EC-PBDAZ-Temp aerogels. (C, G) As-prepared C-PBO-Temp aerogels. (D, H) Carbonized and etched EC-PBO-Temp aerogels. Color coding in each pair (A, E), (B, F), (C, G), and (D, H) represents the various pyrolysis temperatures (Temp), as shown.

Again, specific micropore volumes could be calculated from these data via the Dubinin–Radushkevich (DR) method (Table 2).[52] Pore volumes (Table 2) and pore-size distributions (Figure 3) associated with pore diameters less than 1 nm were also calculated by applying the density functional theory (DFT) method to the CO_2 adsorption isotherms.[55−57] The $V_{micropore}$ volumes via the DR(CO_2) method agreed with the values calculated from the medium- and low-pressure N_2 sorption data (the latter via the DR(N_2) method) only for C-PBO-Temp and EC-PBDAZ-Temp; therefore, for at least these two types of samples, CO_2 uptake can be attributed to a pore-filling mechanism. Nevertheless, $V_{micropore}$ volumes via the DR(CO_2) method were not considered any further in the analysis of the CO_2 absorption because they were not independent of the total CO_2 uptake, which is the subject of this study. Instead, the total CO_2 uptake at 1 atm (equal to the maximum point of the isotherms of Figure 3) was compared with the micropore data (pore volumes, pore sizes, and surface areas) derived from low-pressure N_2 sorption. Micropore volumes calculated from the CO_2 isotherms via the DFT method of analysis (Table 2) were significantly lower than the volumes calculated via all other methods, pointing to the fact that the majority of the "micropores" probed with the various micropore methods were larger than 1 nm and, as we will see shortly, larger even than 2 nm, which is the formal IUPAC cutoff size for micropores, hence our use of quotations with "micropores."

All micropore probing methods point to the fact that etching with CO_2 at 1000 °C dramatically increased the micropore volumes. Starting with the size distribution of the smallest pores probed with the DFT(CO_2) method (<1 nm, Figure 3), it is noted that etching rendered the interior of those pores smoother (the pore size distributions became almost featureless after etching—compare Figure 3F with E, and H with G), the distribution maxima moved to larger values (compare again the same frames in Figure 3), and the cumulative specific pore volumes generally increased after etching (refer to Table 2). Importantly, however, etching opened up/created additional small pores, which are slightly wider than those reflected in the DFT(CO_2) analysis, yet captured, as already discussed, by the rapid rise of the N_2 sorption isotherms at low pressures ($P/P_0 \ll 0.1$). For example, the DFT(CO_2) pore volume of just-carbonized C-PBDAZ-600 and C-PBDAZ-800 was 66–65% of their DR(N_2) pore volume and 24–30% in the corresponding C-PBO-600 and C-PBO-800 aerogels; after etching, however, the DFT(CO_2) pore volume of both EC- systems, at both Temp, dropped down to the 11–17% of their pore volumes calculated via the DR(N_2) method, consistent with the view that etching opened up closed pores and/or created additional small pores, both types being slightly wider than those reflected in the DFT(CO_2) analysis, yet captured by low-pressure N_2-sorption analysis.

"Micropore" volumes, $V_{micropore}$, obtained from low-pressure N_2-sorption data (via the DR(N_2) method were used to calculate average micropore diameters via $4 \times V_{micropore}$/(micropore surface area) (see Table 2). The micropore surface areas used in this formula were calculated via the *t*-plot method (Table 1). ("Micropore" diameters calculated similarly using micropore volumes from the DR(CO_2) method are included in Table 2 for cross-referencing purposes, but again since these values are not independent of the CO_2 uptake, they were not considered any further in the CO_2 absorption analysis.)

The average "micropore" diameters of all carbon and etched-carbon aerogels of this study were in the 2–4 nm range. This range is outside the range of what is formally classified as micropores (<2 nm), thereby, as mentioned above, the term "micropore" is used loosely, referring to the probing methods rather than to actual pore sizes. Looking at those diameters closer and focusing on samples obtained after initial pyrolysis at 600 and 800 °C, we note that the average "micropore"

https://doi.org/10.1021/acs.chemmater.3c01717
Chem. Mater. 2024, 36, 1172−1187

diameters of C-PBDAZ-600_&_800 were in the range of 2.3−2.5 nm; after etching, that average "micropore" diameter in EC-PBDAZ-600_&_800 moved into the 3.0−4.2 nm range. Similarly, the average "micropore" diameters of C-PBO-600_&_800 were in the 2.0−2.8 nm range, and after etching, the average "micropore" diameters of EC-PBO-600_&_800 moved into the 2.7−3.5 nm range. As will be discussed in Section 2.4.a, "micropore" diameters are important in the CO_2 uptake by the C- and EC- aerogels of this study.

2.3. The Chemical Composition of Carbonized and Etched Samples. The chemical composition of all post-oxidation/aromatization samples was probed with combustion CHN analysis. Quantification of the O/N ratio on the surface of these samples was carried out by X-ray photoelectron spectroscopy (XPS). All compositional analysis data are provided in Table S1 of Appendix I in the Supporting Information. As a carryover from the relative composition of PBDAZ versus PBO, all C-PBDAZ-Temp samples contained more N than their PBO counterparts (7−11% versus 5.2−5.7%, respectively—see Table S1a). The amount of oxygen in samples where such a comparison would be meaningful (i.e., for Temp = 600 or 800 °C) was approximately the same among C-PBDAZ-Temp and C-PBO-Temp (7−9%). After etching, EC-PBDAZ-Temp still contained more N than EC-PBO-Temp, but the difference was much smaller than that before etching (3.6 vs 3.0%, respectively). Etching took away N more effectively than O; thus, postetching EC-PBDAZ-Temp still contained about 9% O versus about 8% in EC-PBO-Temp. In summary, both EC-PBDAZ-Temp and EC-PBO-Temp were much richer in oxygen than nitrogen relative to their pre-etching counterparts.

The chemical situation of the heteroatoms in C-PBDAZ-Temp, C-PBO-Temp, EC-PBDAZ-Temp, and EC-PBO-Temp at Temp = 600 and 800 °C was probed with high-resolution XPS (Figures 4 and 5). All O 1s spectra were fitted with two Gaussians. The N 1s spectra of C-PBDAZ-600 and of EC-PBDAZ-600 were fitted with three Gaussians; the corresponding N 1s spectra of C-PBDAZ-800 and of EC-PBDAZ-800 required four Gaussians. The group assignments are listed in Figures 4 and 5.

The common theme in all N 1s spectra is that they looked pairwise (in terms of pyrolysis conditions) similar between the PBDAZ- and the PBO-derived aerogels. Thus, the ratio of the pyridonic-to-pyridinic nitrogen in C-PBDAZ-800 and C-PBO-800 was higher than that in C-PBDAZ-600 and C-PBO-600. That pyridonic-to-pyridinic nitrogen ratio of each material increased significantly after reactive etching with CO_2 at 1000 °C. Overall, the N 1s spectra of both EC-PBDAZ-800 and EC-PBO-800 were all dominated by pyridonic nitrogen. However, there are also some small yet important differences in the N 1s spectra of the PBDAZ- and PBO-derived carbon aerogels: for example, while all PBO-derived carbon aerogels irrespective of pyrolysis temperature (600 or 800 °C), either as-prepared or after etching at 1000 °C under CO_2, consisted only of pyridinic and pyridonic nitrogen (within the constrains just described), the N 1s spectra of the corresponding PBDAZ-derived carbon aerogels included around 26% of nitroxide nitrogen ($-N^+-O^-$ at around 403.4−403.7 eV) and tertiary nitrogen (401.8−402.1 eV).[58] EC-PBDAZ-600 contained only nitroxide (26.1%), while EC-PBDAZ-800 contained both nitroxide (13.6%) and tertiary nitrogen (12.7%).

Those features in the N 1s spectra were accompanied by parallel changes in the O 1s spectra (Figures 4 and 5). All O 1s

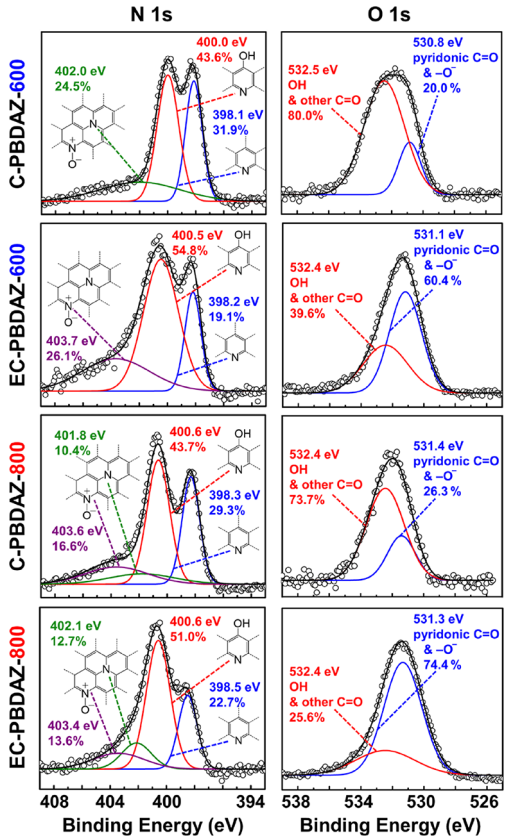

Figure 4. High-resolution N 1s and O 1s XPS spectra of PBDAZ-derived carbon (C−) and etched carbon (EC−) aerogels. Primary data were fitted with Gaussians, as shown.

spectra were fitted with two Gaussians. The peak at 530.8−532.6 was assigned to pyridonic C═O and alkoxide type of $-O^-$,[58] and its intensity increased whenever the amounts of pyridonic nitrogen and nitroxide increased (see previous paragraph); thus, that peak was always more intense in the EC samples and reached its maximum contribution in the EC-PBDAZ-800 samples (74.4%). The increased contribution of the pyridonic/$-O^-$ functionality, and the concurrent reduction of the amount of N in etched samples was accompanied by a higher CO_2 uptake, as it will be discussed in Section 2.4.a. The second deconvoluted peak in all the spectral O 1s (532.4−533.6 eV) was attributed to OH and/or amide-type carbonyls (refer to the aromatized structures in Scheme 1).

2.4. PBDAZ- and PBO-Derived Carbon and Etched Carbon Aerogels as CO_2 Absorbers. *2.4.a. The CO_2 Uptake.* All of the CO_2 absorption isotherms (Figure 3) were reversible with no hysteresis. The CO_2 uptake data at 273 K and 1 bar (P/P_0 = 0.03) from the various C and EC aerogels of this study are summarized in Table 2 under the heading "Measured" and were taken as the maxima along the corresponding CO_2 adsorption isotherms of Figure 3. Overall, all etched carbon aerogels showed higher CO_2 uptake capacities than their corresponding carbon precursors, and C- and EC-PBDAZ-Temp aerogels showed higher CO_2 uptakes (up to more than double those of the corresponding PBO samples. Specifically, for Temp in the range 600−800 °C, C-PBO-Temp showed CO_2 uptakes from 2.8 to 3.0 mmol g^{-1} while C-PBDAZ-Temp aerogels absorbed in the range 5.5−7.0 mmol g^{-1}. All these values fall within what has been observed before for other carbon aerogels. On the other hand, however,

https://doi.org/10.1021/acs.chemmater.3c01717
Chem. Mater. 2024, 36, 1172−1187

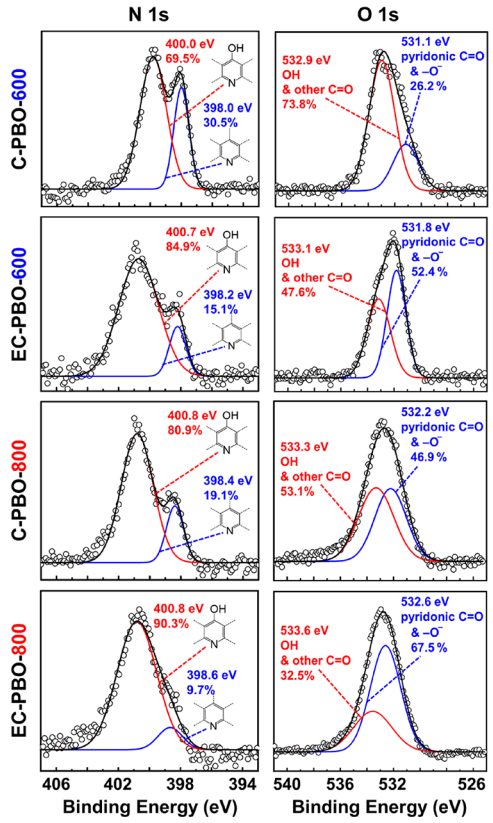

Figure 5. High-resolution N 1s and O 1s XPS spectra of PBO-derived carbon (C−) and etched-carbon (EC−) aerogels. Primary data were fitted with Gaussians as shown.

EC-PBDAZ-Temp aerogels showed CO_2 uptake capacities in the range of 10.2−11.5 mmol g^{-1} while the absorption capacity of EC-PBO-Temp aerogels lagged significantly behind, falling in the range of only 4.4−4.6 mmol g^{-1}. It is noted that the CO_2 uptake capacities measured for EC-PBDAZ-Temp were higher than the values reported under the same conditions (273 K, 1 bar) for other good carbon-based CO_2 absorbers in the literature, such as phenolic-based activated carbon microspheres (8.9 mmol g^{-1})[59] and carbon nanotubes (4.8 mmol g^{-1}),[60] and they fall in the range of other phenolic resin-derived and CO_2-etched carbon aerogels (14.8 mmol g^{-1}).[48]

Using as a point of departure the fact that the highest CO_2-uptake values were associated with samples having high micropore surface areas, and high micropore volumes (refer to Table 2), the measured CO_2 uptake of every sample was compared with (a) the monolayer coverage of its entire BET surface area with CO_2 (assuming 0.17 nm^2 per CO_2 molecule);[55] (b) the monolayer coverage of only its micropore surface area; and (c) complete filling of its DR(N_2) micropore volume with liquid CO_2 (density of liquid CO_2 = 1.023 g cm^{-3}).[54,61] Calculated values according to a−c are included in Table 2. It is noted again that since micropore volumes obtained via the DR(CO_2) method are linked to the overall CO_2 uptake, which may be related not only to the actual micropore volume but also to the thermodynamics of the interaction of the CO_2 with the surface of the micropores, only the DR(N_2) volumes were considered for calculating the amount of CO_2 needed for (c).

Focusing on just-carbonized C-PBDAZ-Temp aerogels, their CO_2 uptake was higher than the amount of CO_2 required for complete coverage of their entire BET surface area and therefore their micropore surface areas as well. Clearly, the CO_2 uptake by those materials was not a simple surface adsorption phenomenon. On the contrary, the CO_2 uptake by just-carbonized C-PBO-600 and C-PBO-800 was *lower* than the amount of CO_2 required for complete coverage of the BET surface area and about equal to the amount required for complete monolayer coverage of their micropores (Table 2). Furthermore, since the micropore characteristics (volumes, sizes, and surface areas) of all just-carbonized samples (namely, of C-PBDAZ-Temp and C-PBO-Temp, Temp = 600 and 800 °C) were quite similar between the two groups of materials (see Tables 1 and 2), we conclude that the different amounts of CO_2 uptaken (5.5−7.0 and 2.8−3.0 mmol g^{-1}, respectively) were related to the chemical lining of the micropores and its interaction with CO_2.

Shifting attention to the etched carbon aerogels, the amounts of CO_2 uptaken by the various EC-PBDAZ-Temp were close to one another consistent with the fact that the final etching step was an equalizer in terms of material properties relevant to CO_2 uptake. The same observation was valid for EC-PBO-Temp. The order of the measured amount of CO_2 uptaken and the amount needed for complete coverage of the BET surface area of EC-PBDAZ-Temp was reversed relative to what was observed with the just-carbonized samples: despite the dramatic increase of the BET surface areas of all EC-PBDAZ-Temp and EC-PBO-Temp materials relative to their C precursors (Table 1), the CO_2 uptake remained significantly lower than the amounts calculated for monolayer coverage of the entire BET surface areas for all materials with CO_2 (Table 2). This, together with the 3.5-fold increase in the DR(N_2) "micropore" volume after etching, led to the conclusion that the increased CO_2 uptake by etched samples was a phenomenon related to the micropore structure and/or surface chemistry. In the case of EC-PBDAZ-Temp, etching increased not only the DR(N_2) micropore volume but also the "micropore" size, sending the new pore diameters into the 3.6−4.2 nm range. Nevertheless, the CO_2 uptake was also much lower than the amount of CO_2 needed to fill the DR(N_2) volumes of all of the etched samples. In fact, the CO_2 uptake by all EC-PBDAZ-Temp samples was close to the amount calculated for monolayer coverage of the micropore surface areas with CO_2 (Table 2). However, as discussed below, this monolayer/micropore coverage model is not consistent with all available data for EC-PBDAZ-Temp and EC-PBO-Temp. In the case of EC-PBO-Temp, pore sizes did not increase much after etching (moving into the 2.7−2.8 nm range from 2.0 to 2.5 nm pre-etching, Table 2); therefore, it was concluded that the postetching 3.5-fold increase in the micropore volume was mostly due to an increase in the number of pores rather than rendering the existing ones wider. This model suggests that etching opened the porosity up, as supported by the skeletal density data (see Section 2.2.a). Nevertheless, the CO_2 uptake by EC-PBO-Temp (4.35−4.60 mmol g^{-1}) remained less than half of the uptake by EC-PBDAZ-Temp (10.2−11.5 mmol g^{-1}) despite comparable micropore volumes (Table 2) and comparable surface areas (Table 1). In fact, the CO_2 uptake by EC-PBO-Temp remained about 4× lower than what was needed to fill their DR(N_2) micropore volume and more than 2× lower than what was need for monolayer coverage of the micropore surface areas with CO_2 (Table 2). Given the similar chemical compositions of EC-PBO-Temp and EC-PBDAZ-Temp (see Section 2.3), the different CO_2 uptake properties of the two

https://doi.org/10.1021/acs.chemmater.3c01717
Chem. Mater. 2024, 36, 1172−1187

materials must be related either to the small differences in the functional group lining of the "micropores", or to the smaller pore sizes of EC-PBO-Temp. In that regard, it is accepted that CO_2 entering the confined space of small pores loses its translational degrees of freedom and, therefore, subsequent adsorption of CO_2 on the pore walls is an isoentropic process.[62−65] Thus, the uptake of CO_2 in micropores is influenced by an interplay of the pore size and the enthalpy of the interaction of CO_2 with the functional groups lining the surface of the micropores.

An insight into the interaction of CO_2 with the micropore surfaces of each carbon aerogel of this study is provided by the isosteric heat of adsorption, Q_{st}, which is the negative of the differential change in the enthalpy of adsorption and was calculated as a function of the CO_2 uptake by employing simultaneous virial fitting of the CO_2 adsorption isotherms at two temperatures (273 and 298 K—refer to Section 4.2 and Figure S1 of Appendix II in the Supporting Information).[66] All fitting data are given in Table S2 of Appendix II in the Supporting Information. The Q_{st} plots as a function of the amount of uptaken CO_2 for all carbonized and etched samples are shown in Figure 6.

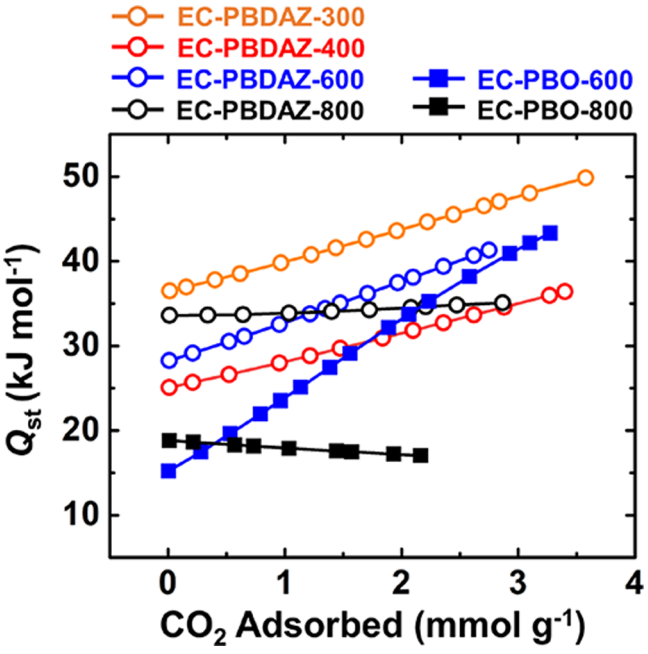

Figure 6. Isosteric heats of CO_2 adsorption (Q_{st}) by EC-PDBAZ-Temp and EC-PBO-Temp.

The energy of the interaction of CO_2 with the surface of each adsorbate is referred to as Q_0 and is given by the intercepts of the Q_{st} plots at zero CO_2 uptake. Generally, higher Q_0 values (e.g., >40 kJ mol^{-1}) come from chemisorption while lower Q_0 values from physisorption.[67,68] It is speculated that chemisorption and physisorption favor different orientations of CO_2 relative to the surfaces of the "micropores". Three such possible interactions and orientations of CO_2 relative to the surface of the "micropores" of the carbon aerogels of this study are shown in Scheme 3 and are discussed below.

The Q_0 values for the carbon aerogels of this study are summarized in Table 2. The Q_0 values of all C samples were in the range 19−23 kJ mol^{-1}. Similarly, the Q_0 values of the two

Scheme 3. Possible Interactions and Orientations of CO_2 Relative to the Surface within Micropores

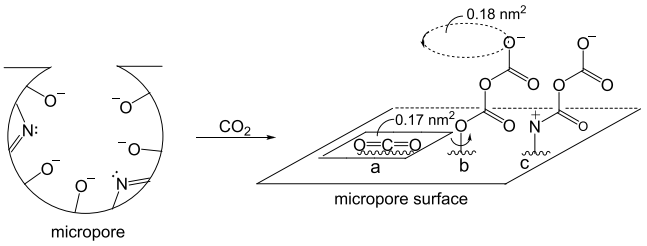

EC-PBO-600_or_800 aerogels were 15 and 19 kJ mol^{-1}, respectively, suggesting physisorption, e.g., via interaction of quadrupolar CO_2 with quadrupolar "N"-rich sites inside the micropores.[69] The geometry that maximizes this interaction is the flat-down configuration "a" in Scheme 3.[66] Yet, as also mentioned above, the CO_2 uptake by EC-PBO-600_or_800 was less than half of what was needed for monolayer micropore coverage. This is attributed to a combination of the low "N" content of these materials (see Section 2.3) and their smaller pore diameters that may impose restrictions on the development of configurations "b" and "c" of Scheme 3. On the other hand, the Q_0 values of the EC-PBDAZ-Temp aerogels were in the 27−38 kJ mol^{-1} range, which could be attributed to weak chemisorption. Indeed, reasoning by analogy to (a) the formation of carbamate as the primary adduct upon CO_2 capture by amine solutions,[70−72] or by dry amine-bearing surfaces,[73,74] and (b) the formation of bicarbonate via reaction of CO_2 with HO^- in amine solution,[70−72] or on wet amine-bearing surfaces,[73] weak chemisorption here is expected to involve nucleophilic attack of surface-N: (pyridinic or pyridonic) or of surface-O^- (an as-good or better electrophile as HO^-) onto CO_2 yielding surface-bound carbamate and carbonate moieties, respectively. The orientations of CO_2 in those surface-bound adducts are designated as structures "b" and "c" in Scheme 3. Based on bond energies,[75] the enthalpic change of the reaction of CO_2 with surface $-O^-$ via this process is nearly neutral.[48] On the other hand, the reaction of CO_2 with surface −N: (pyridinic or pyridonic) is slightly endothermic (by about 17 kcal mol^{-1});[48] therefore, of the two processes, "b" or "c", the former is more favorable. Interestingly, the exclusion area (shown by a dashed oval in Scheme 3) by pivoting around the point of attachment of a two-CO_2 branch is 0.18_5 nm^2, i.e., similar to the area occupied by a single CO_2 molecule lying flat on the surface. However, to accommodate this dimer-like adduct lengthwise, pores must be wider. Therefore, according to this model, wherein N favors geometry "a" and surface alkoxides favor geometry "b", carbon aerogels with (a) more surface $-O^-$ groups and less nitrogen (case of all etched samples either from PBO or PBDAZ—refer to Table S1 of Appendix I in the Supporting Information) should uptake more CO_2, provided that (b) pores are wider (case of all EC-PBDAZ-Temp—Table 2). Data suggest that both factors (a) and (b) act together.

Further support for the proposed modes of interaction of CO_2 with "micropores" is provided by the shape of the Q_{st} plots (Figure 6). As the CO_2 uptake increased, the Q_{st} plots of EC-PBDAZ-Temp aerogels (Temp ≤600 °C) trended slightly upward or stayed flat (case of EC-PBDAZ-800). These trends are consistent with weaker physisorption type of interactions in the beginning (structure "a" of Scheme 3), switching to structure "b" as more CO_2 was forced in the pores with

https://doi.org/10.1021/acs.chemmater.3c01717
Chem. Mater. 2024, 36, 1172−1187

increasing pressure and as CO_2 had to accumulate on already surface-bound CO_2. In the case of EC-PBDAZ-800, whose surfaces are more O-rich (O/N atomic ratio = 1.63 compared to 1.05−1.11 of the other EC-PBDAZ-Temp aerogels), it is speculated that pore-filling started off with significant contributions from structure "b" and therefore further accumulation of CO_2 proceeded with near-zero enthalpy change. Similar reasoning can be applied to the Q_{st} plots of EC-PBO-800, which was more O-rich than EC-PBO-600 (O/N ratio: 1.37 vs 1.08, respectively). While the Q_{st} plot of EC-PBO-600 trended upward, the Q_{st} plot of EC-PBO-800 remained substantially flat. Overall, the pairwise analogous chemical lining of the surfaces of the various carbon aerogels of this study creates similar trends in the initial CO_2 uptake by all materials; thereby, the higher CO_2 uptake by EC-PBDAZ-Temp versus EC-PBO-Temp at 1 bar (Figure 3) is a phenomenon that has to be reconciled with their wider "micropores" that could accommodate more "b"-type dimer-like CO_2 adducts (Scheme 3) until optimal occupancy.

To probe further the chemical situation of CO_2 in the micropores (Scheme 3), we reviewed options we reviewed several experimental options. Amine adducts of CO_2 in solution are identified with insertion-probe IR.[71] CO_2 on amine-modified silica has been probed with transmission IR.[73] Those IR methods are not easily adoptable to probe carbon aerogels under CO_2. Isotope-enriched $^{13}CO_2$ captured by certain amine-modified MOFs has been looked at with solid-state ^{13}C NMR.[74,76,77] In terms of carbon adsorbers, their ^{13}C NMR spectrum in the aromatic region is expected to be broad, spanning the 100−150 ppm range[78] and rendering observation/identification of $^{13}CO_2$ adducts challenging. Here, it was reasoned that a good approach to looking at the interaction of CO_2 with carbon aerogels would involve techniques that allow probing a sample in a closed environment under CO_2 from a distance, e.g., with a laser beam. Recently, by extrapolation of surface-enhanced Raman spectroscopy, this technique has been adopted quite successfully in the study of adsorption of gases (e.g., CO_2, hydrocarbons) on microporous adsorbers.[79−82] Typically, such studies involve substrates that uptake CO_2 at high pressures; thereby, they use special cells wherein adsorption creates additional satellite peaks at slightly lower energies (by 4−6 cm^{-1}) relative to the main gas-phase scattering events of CO_2 in the 1200−1450 cm^{-1} range.[79] Motivated by these literature reports, we opted for Raman spectroscopy, and our experimental setup is shown in Figure 7A. A piece of dry ice was placed near the closed end of a 1″-diameter test tube held horizontally on the stage of the Raman spectrometer. A piece of freshly dehydrated carbon aerogel (150 °C overnight) was placed near the other end of the tube that was vented with a needle through a rubber septum. This setup ensures atmospheric pressure in the tube, i.e., the highest pressure in all other CO_2 adsorption experiments in this study. The sample temperature in this configuration was measured at around 10 °C with a handheld laser-guided probe. Figure 7B shows the Raman spectra of three carbon aerogels from this study in open air (room temperature). All three materials showed weak D and G bands of disordered graphite at 1371 and 1592 cm^{-1}.[83] Figure 7C includes the spectrum of solid CO_2 taken by focusing the laser beam on the piece of the dry ice in the tube, as well as the spectra of the three carbon aerogels of Figure 7B under CO_2 (in the setup of Figure 7A). The spectrum of the dry ice was the same as the spectrum of CO_2 in the gas phase.[79] On the other hand, under CO_2, the

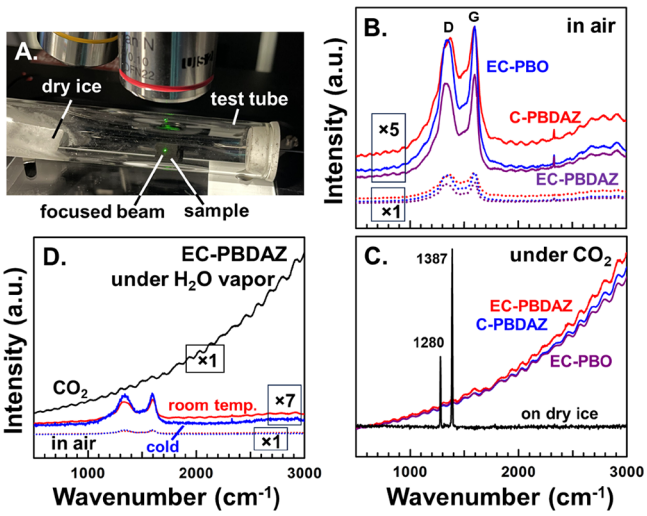

Figure 7. (A) Experimental setup for recording the Raman spectra of carbon aerogels under CO_2. (B) Color-coded Raman spectra in air of three carbon aerogel samples from this study, as shown. The Intensity scale of the upper three spectra was five times more sensitive. (C) The same samples were used as in frame B under CO_2. The frame includes the Raman spectrum of dry ice (black line). All spectra were taken and recorded as the "×1" spectra of frame B. (D) Raman spectrum of EC-PBDAZ under CO_2 and in air after moisture absorption from a water vapor saturated environment. The spectrum under CO_2 is reported under the same conditions as the "×1" spectra in air.

background scattering on the carbon aerogels was intensified and drifted upward with increasing wavenumber; neither the bands of graphite nor those of any other CO_2-related vibrations were discernible. (Note that the spectra of Figure 7C and the spectra designated as ×1 spectra in Figure 7B were taken under the same conditions of laser power and aperture time.) Subsequently, in order to test whether somehow water getting absorbed on the carbon aerogels could be responsible for the observations of Figure 7C, in another experimental configuration, a few water drops were placed at the far end of the test tube and an EC-PBDAZ aerogel piece was allowed to equilibrate with the water vapor at room temperature overnight (the test tube was kept slightly inclined, and its open end was closed with a rubber septum). The sample absorbed water vapor, and its weight increased by about 100%. Raman spectra were obtained with the setup at this configuration at room temperature, and by surrounding and "burying" the test tube in dry ice (referred to as "cold"). In both configurations, only the D and G bands of disordered graphite were discernible at practically the same intensity (Figure 7D). By placing a piece of dry ice at its usual place (the small water pool still being in place froze instantly), the Raman spectrum showed the familiar (refer to Figure 7C) intensified and upward drifting background. The increase of the background intensity under CO_2 in Figure 7C,D was attributed to a strong speckle effect,[84] resulting from a dramatic increase in the diffuse reflectance from the surface of the carbon aerogels due to newly created randomly oriented highly efficient nanoscopic reflectors. The ripples noted on the background were identical before and after exposure to CO_2, they were independent of the type of the material or whether observation took place directly or through the glass tube, and therefore, they were attributed to an instrument artifact. The upward drift of the background with increasing wavenumber was probably due to superimposed Rayleigh scattering.

https://doi.org/10.1021/acs.chemmater.3c01717
Chem. Mater. 2024, 36, 1172−1187

According to Figure 7D, adsorbed water vapor did not seem to interfere quantitatively with the CO_2 adsorption. Furthermore, the Raman spectra obtained in the configuration of Figure 7A of other nonmicroporous carbon and graphitized carbon aerogels that do not adsorb CO_2 quantitatively (e.g., aerogels derived from fibrous polyimide aerogels[37]—unpublished results) were a superposition of strong graphite bands and low-intensity CO_2 bands like those on dry ice (Figure 7C). Consistent with all data considered together, the increased diffuse reflectance of the carbon aerogels of this study under CO_2 was attributed to quantitative micropore filling with CO_2; the CO_2-filled micropores became nanoscopic reflectors responsible for the speckle effect. All control experiments suggest that most pore-filling CO_2 should be in forms other than O═C═O, such as in species "b" and "c" of Scheme 3.

2.4.b. Toward Practical Applications: Reusability and Selectivity for CO_2 toward Other Gases. The high CO_2 uptake capacity for PBDAZ-derived carbon aerogels, and the first clues we saw in the last paragraph about their indifference to water vapor as far as CO_2 uptake is concerned, encourages further consideration of this type of material for practical use. However, although a high CO_2 uptake capacity is a necessary condition for applications, it is hardly sufficient: reusability and a high selectivity for CO_2 toward other gases are also necessary. Reusability was demonstrated over five in-tandem absorption/desorption cycles using the best performer (albeit marginally) among all samples of this study: EC-PBDAZ-300 (refer to Figure 3). Results are presented in Figure 8A. The variation in the maximum CO_2 uptake value is considered to be within error.

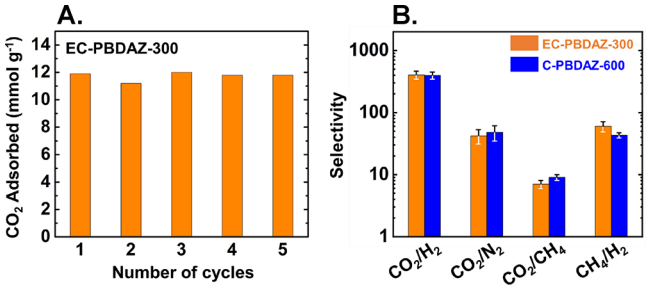

Figure 8. (A) Sorbent reusability is demonstrated over five cycles for one of the best performers of this study (refer to Figure 3B). The sample was degassed at 80 °C/12 h under vacuum between runs. (B) Relative selectivity at 273 K of EC-PBDAZ-300 (orange) and C-PBDAZ-600 (blue) toward CO_2 as compared to other gases as indicated. Error bars reflect averages of at least three measurements using three separate samples.

On the other hand, CO_2 absorbers for precombustion CO_2 capture should be selective against CH_4 and H_2, while for postcombustion capture, they should be selective against N_2. Two samples (C-PBDAZ-600 and EC-PBDAZ-300) with the highest CO_2 uptake capacity from each category of this study (Figure 3) were selected for evaluating their selectivity toward CO_2 relative to other gases. Advanced-stage selectivity studies typically involve uptake from mixtures of gases. Initial selectivity studies are conducted by comparing the initial slopes of the isotherms of two competing gases, assuming that at low coverages, the gas uptake conforms to Henry's law.[85−87] The adsorption isotherms of C-PBDAZ-600 and EC-PBDAZ-300 for CH_4, N_2, and H_2 at 273 K are shown in Figure S2 of Appendix III in the Supporting Information. Henry's constants (K_H = initial slopes) for each gas were calculated by fitting these isotherms with virial-type equations, as described in Section 4.2. Selectivities were then calculated as the ratios of Henry's constants and are shown in bar-graph form in Figure 8B. Low uptakes of N_2 and H_2 at 273 K by both just-carbonized and etched carbon aerogels resulted in low K_H values and high selectivity for CO_2 toward those two gases. The relatively higher uptake of CH_4, and thereby the lower selectivity for CO_2 versus CH_4, was due to its high polarizability.[88] As shown in Figure 8B, the selectivity of EC-PBDAZ-300 and C-PBDAZ-600 aerogels for CO_2 versus H_2 was 404 ± 60 and 397 ± 52, respectively; the corresponding selectivity of both materials for CO_2 versus N_2 was in the range 42−48 and in the range only 7−9 versus CH_4. This proximity of the selectivity values of PBDAZ-derived carbon aerogels before and after etching is noteworthy. Selectivity through Henry's constants reflects low-pressure behavior, including of course during first-layer coverage, which is sensitive to the interactions of the adsorbate with the absorber walls. According to the XPS data of Figure 4, in terms of functional groups involving N (but not in terms of O), the surfaces of C- and EC-PBDAZ were similar; therefore, low-pressure selectivity values support the quadrupolar physisorption type of initial interaction of CO_2 with the micropore surfaces (structure "a"—Scheme 3), as discussed in the previous section in relation to that from the Q_{st} plots. Interestingly, the trends in the selectivity values before and after etching of PBDAZ- and PBO-derived carbon and etched carbon aerogels (from this study and ref 48, respectively) do not seem to match one another, but further speculation is risky. Overall, PBDAZ-derived carbon aerogels with high absorption capacity and selectivity toward CO_2 and no sign of saturation up to 1 bar are potential candidates for application in CCS. Specifically, the high selectivity of EC-PBDAZ for CO_2 versus H_2 (up to 404:1) is relevant to precombustion capture of CO_2, and the high selectivity for CO_2 versus N_2 (up to 48:1) is relevant to postcombustion CO_2 capture.

3. CONCLUSIONS

Despite their structural analogy and similar pyrolytic behavior, PBDAZ and PBO aerogels yield carbon aerogels with quite different CO_2 uptake capacities (up to 7.0 mmol g^{-1} versus only 3.0 mmol g^{-1}, respectively, at 273 k, 1 bar). This difference is amplified after pyrolytic activation (etching) with CO_2 at 1000 °C, reaching values up to 11.5 mmol g^{-1} for etched carbon aerogels derived from PBDAZ aerogels versus only up to 4.6 mmol g^{-1} from corresponding materials derived from PBO aerogels. Although PBDAZ aerogels contained only N heteroatoms, while PBO aerogels contained both oxygen and nitrogen, the higher CO_2 uptake capacities of the PBDAZ-derived carbon aerogels could not be attributed to that stoichiometric difference. This is because quantitative carbonization requires prior oxidative aromatization of either polymer, which introduces oxygen into both materials; later, reactive etching removes nitrogen preferentially, yielding carbon aerogels with approximate similar elemental and functional group composition irrespective of their source. On the other hand, all carbon aerogels from either polymer aerogel, PBDAZ or PBO, include micropores. CO_2 entering those pores loses its translational degrees of freedom; thereby, for the correct size of pores, the CO_2 uptake can be an entropy-neutral enthalpy-only-driven process. According to the data presented here, and elsewhere,[31] that pore size has an

https://doi.org/10.1021/acs.chemmater.3c01717
Chem. Mater. 2024, 36, 1172−1187

upper bound in the range of 3−4 nm. Once CO_2 enters these pores, the uptake capacity is related to its interaction with the pore walls, with CO_2 having already entered the pores and the crowding within the pores. Considering all data together, high CO_2 uptake capacities are related to the amount of oxygen (pyridonic and nitroxide) lining the pore surfaces. The presence of nitrogen seems to be less important. A more favorable CO_2 uptake, even from pores lined with less oxygen but already partially occupied by CO_2, is attributed to the energy-neutral reaction of CO_2 with surface−O−(C═O)−O^- carbonate groups toward surface-bound carbonate dimers: surface−O−(C═O)−O−(C═O)−O^-. For steric reasons, this sequence of events is favored by pores near the upper bound of suitable pore sizes (3−4 nm) and is used to explain the high levels of CO_2 uptake by PBDAZ-derived carbonized and etched aerogels. In addition to high CO_2-uptake capacities, etched carbon aerogels derived from PBDAZ show high selectivity for CO_2 versus H_2 (up to 404:1), which is relevant to precombustion CO_2 capture, and high selectivity for CO_2 versus N_2 (up to 48:1), which is relevant to postcombustion CO_2 capture.

4. EXPERIMENTAL SECTION

4.1. Materials. All reagents and solvents were used as received unless noted otherwise. Siphon grade CO_2, CO_2 (99.999%), argon (99.999%), N_2 (99.999%), H_2 (99.999%), and CH_4 were purchased from Ozark Gas (Rolla, Missouri). Liquid N_2 and O_2 (99.999%) were purchased from Air Gas (St. Louis, Missouri). The propane hand torch cylinder (87.5−100%) was purchased form BernzOmatic (Newark, New Jersey). The benzodiazine (BDAZ) monomer and the benzoxazine (BO) monomer were prepared as published previously.[34,45]

Preparation of Polybenzodiazine and Polybenzoxazine Aerogels (PBDAZ and PBO). In a typical procedure, the BDAZ monomer (20% w/w) or the BO monomer (7 wt %) was dissolved in DMF. Concentrated aq. HCl (12.1 N) was added to those solutions as catalyst at a concentration of 4.0% w/w and 4.5% w/w for the BDAZ and BO monomers, respectively. The resulting sols were stirred at room temperature for 10 min and then poured into molds. The BDAZ sol was placed in an oven for gelation at 100 °C for 3 days, while the BO sol was left for gelation at RT for 5 h. At the end of the corresponding periods, wet gels were removed from the molds and were washed successively with DMF (PBDAZ gels were washed eight times, PBO gels were washed two times) and then with acetone (PBDAZ gels were washed six times, and PBO gels were washed four times). The amount of solvent used for each wash was 4× the volume of the gel. Finally, wet gels were dried in an autoclave with liquid CO_2 taken out at the end as an SCF. The resulting as-prepared aerogels are termed PBDAZ and PBO.

Oxidative Aromatization of PBDAZ and PBO Aerogels to PBDAZ-240 and PBO-200, Respectively. As-prepared PBDAZ aerogel monoliths were transferred to a tube furnace. The temperature of the furnace was raised to 240 °C at 2.5 °C min^{-1} under flowing O_2 (0.3 L min^{-1}) and remained under these conditions for 24 h. As-prepared PBO aerogels were heated at 200 °C in air for 24 h in an oven. The resulting aerogels are termed PBDAZ-240 and PBO-200, respectively.

Pyrolytic Conversion of Aromatized PBDAZ-240 and PBO-200 Aerogels to Carbon Aerogels (C-PBDAZ-Temp and C-PBO-Temp). Aromatized PBDAZ-240 aerogel monoliths were placed in the tube furnace under flowing argon (0.3 L min^{-1}) and were heated (2.5 °C min^{-1}) for 5 h at either 300, 400, 600, or 800 °C. The resulting aerogels are referred to as C-PDBAZ-Temp. Similarly, PBO-200 were pyrolyzed similarly at either 600 or 800 °C and the resulting aerogels are referred to as C-PBO-Temp. ("Temp" in the sample names denotes the pyrolysis temperature.)

Reactive Etching of C-PBDAZ-Temp and C-PBO-Temp Aerogels to Etched Carbon Aerogels (EC-PBDAZ-Temp and EC-PBO-Temp). The C-PBDAZ-Temp or the C-PBO-Temp aerogels were placed in the tube furnace and were heated to 1000 °C under continuous flow of Ar; once at temperature, the flowing gas was switched to CO_2 (0.3 L min^{-1}) for 3 h and then back to Ar. All heating and cooling of the tube furnace were conducted at a rate of 2.5 °C min^{-1}. The resulting aerogels are referred to as EC-PBDAZ-Temp and EC-PBO-Temp, respectively.

4.2. Methods. *Drying Wet Gels into Aerogels.* Drying wet gels into aerogels was carried out in an autoclave (SPI-Dry Jumbo Supercritical Point Dryer, SPI Supplies, Inc., West Chester, Pennsylvania). Samples were placed in the special boat supplied with the autoclave, and acetone was added until the samples were submerged. The boat was loaded to the autoclave that was kept at 14 °C. The pressure vessel was closed, and liquid CO_2 was allowed in multiple times, and each time it was drained out through a valve at the bottom of the autoclave. The cycle was repeated until all acetone was extracted from the pores of the samples completely. The end-of-process criterion was that CO_2 released through the drain valve formed dry ice immediately. Subsequently, the temperature of the autoclave was raised to 40 °C. After staying at that temperature for 1 h, 1 h, supercritical fluid (SCF) CO_2 was vented off as a gas over a period of 5 h.

Pyrolysis and Etching. All pyrolytic processes were conducted in a tube furnace (MTI GSL1600X-80). The heating rate was always 2.5 °C min^{-1}, and the gas (argon, oxygen, or carbon dioxide) flow rate was always set at 0.3 L min^{-1}.

Physical Characterization. Bulk densities (ρ_b) were calculated from the weight and physical dimensions of the samples. Skeletal densities (ρ_s) were measured using helium pycnometry with a Micromeritics AccuPyc II 1340 instrument.

Chemical Characterization. CHN elemental analysis was conducted either in-house with an Exeter Analytical Model CE440 elemental analyzer calibrated with acetanilide, urea, and glycine and with its combustion furnace operated at 1050 °C, or at Galbraith Laboratories (Knoxville, Knoxville 37921). X-ray photoelectron spectroscopic analysis (XPS) was carried out with a Thermo Fisher Scientific Nexsa X-ray Photoelectron Spectrometer System. Samples were mixed and ground together with Au powder (5 wt %) as an internal reference. Deconvolution of the spectra was performed with Gaussian function fitting by using the OriginPro 9.7 software package. Raman spectroscopy was conducted with an XplorA PLUS Confocal Raman Microscope equipped with an air-cooled 532 nm solid-state 100 mW laser and a TE air-cooled CCD detector (Horiba Instruments, Inc., Piscataway, New Jersey). All experiments were conducted with the laser power set at 25% of its maximum.

Microstructural Characterization. Scanning electron microscopy (SEM) was conducted with Au-coated samples on a Hitachi Model S-4700 field-emission microscope.

Porosity and Gas Sorption Studies. The pore structure was probed with N_2-sorption porosimetry at 77 K using either a Micromeritics ASAP 2020 instrument equipped with a low-pressure transducer or a TriStar II 3020 version 3.02 surface area and porosity analyzer. Before analysis, samples were degassed for 24 h under a vacuum at 80 °C. Total surface areas, σ, were determined via the Brunauer−Emmett−Teller (BET) method from the medium-pressure N_2-sorption isotherms. Pore size distributions for pores in the mesopore and low macropore range were obtained using the BJH method applied on the desorption branch of the medium-pressure N_2 sorption data (up to 1 bar, i.e., as $P/P_0 \rightarrow 1$). Micropore surface areas were calculated via *t*-plot analysis of the medium-pressure N_2-sorption isotherms using the Harkins and Jura model.[51] More detailed micropore analysis was conducted with low-pressure N_2 sorption at 77 K using the Micromeritics ASAP 2020 instrument and N_2-sorption data obtained with the low-pressure transducer, or with CO_2 adsorption up to 760 Torr (relative pressure P/P_0 = 0.03) at 273 K using the Micromeritics TriStar II 3020 system mentioned above. Prior to low-pressure N_2-sorption analysis at 77 K, a special degassing step was carried out under 1 μm Hg at 120 °C *directly on the analysis*

https://doi.org/10.1021/acs.chemmater.3c01717
Chem. Mater. 2024, 36, 1172−1187

port of the Micromeritics ASAP 2020 instrument. For the CO_2 adsorption studies, samples were degassed in their sample tubes below 20 mTorr at 120 °C for 16 h using a Micromeritics VacPrep 061 sample degassing system. Typically, just before the CO_2 analysis, the instrument measures the free space in the sample tube via an automated process using helium and then proceeds with the CO_2 uptake analysis as a function of pressure. However, to avoid the possibility that any residual helium might be retained in the tiniest of the pores, thus reducing the rate of CO_2 uptake by the material, the free space was measured separately. For this, first the instrument was allowed to measure the free space using helium; subsequently, the sample tubes were degassed again on the degassing system and then they were put back on the TriStar 3020 instrument for the CO_2 analysis. This sequence bypasses the automatic measurement of the free space, which is entered manually using the value measured just before the second degassing process. Micropore volumes were obtained with the Dubinin–Radushkevich[52] and with the Horvath–Kawazoe method[53] both applied to the low-pressure N_2-sorption data at 77 K, as well as with the Dubinin–Radushkevich method applied to CO_2 adsorption data at 273 K. Pore size distributions for pores <1 nm in size were obtained with DFT applied to the CO_2 adsorption isotherms.[55−57]

Isosteric Heats of CO_2 Adsorption (Q_{st}). Q_{st} values were calculated using the virial fitting method.[66] For this, the CO_2 adsorption isotherms at 273 and 298 K were fitted simultaneously with a virial-type eq 1 using the OriginPro 2020 9.7.0 software package. [P is the pressure in Torr, N is the adsorbed amount in mmol g^{-1}, T is the absolute temperature, a_i and b_i are the virial coefficients, and m and n are the number of coefficients needed to fit the isotherms adequately.] Using the least-squares method, the values of m and n were varied until the sum of the squared deviations of the experimental points from the fitted isotherm was minimized. In all cases, this condition was reached m = 3 and n = 1 (see Table S2 of Appendix II in the Supporting Information). The values of a_o to a_m were introduced into eq 2, and the isosteric heats of adsorption (Q_{st}) were calculated as a function of the surface coverage (N).[P is the pressure in Torr, N is the adsorbed amount in mmol g^{-1}, T is the absolute temperature, a_i and b_i are the virial coefficients, and m and n are the number of coefficients needed to fit the isotherms adequately.] Using the least-squares method, the values of m and n were varied until the sum of the squared deviations of the experimental points from the fitted isotherm was minimized. In all cases, this condition was reached m = 3 and n = 1 (see Table S2 of Appendix II in the Supporting Information). The values of a_o to a_m were introduced into eq 2, and the isosteric heats of adsorption (Q_{st}) were calculated as a function of the surface coverage (N).

$$\ln P = \ln N + \frac{1}{T}\sum_{i=0}^{m} a_i N^i + \sum_{i=0}^{n} b_i N^i \tag{1}$$

[R is the gas constant (8.314 J mol^{-1} K^{-1}) and Q_{st} is obtained in kJ mol^{-1}]. The common term in eq 2 for all N, Q_0, corresponds to i = 0 and is given by eq 3

$$Q_{st} = -R\sum_{i=0}^{m} a_i N^i \tag{2}$$

Q_0 is the heat of adsorption as the coverage goes to zero and is a sensitive evaluator of the affinity of the adsorbate for the surface.

.

$$Q_0 = -Ra_0 \tag{3}$$

Relative Selectivities. Relative adsorption studies for CO_2, CH_4, N_2, and H_2 were conducted with a Micromeritics TriStar II 3020 surface area and porosimetry analyzer at 273 K up to 1 bar. The selectivity for one gas versus another was calculated as the ratio of the respective Henry's constants, K_H. The latter were calculated via another type of virial model, whereas the single-component adsorption isotherms for each gas at 273 K were fitted according to eq 4.[87]

$$\ln N = \ln P + K_1 + K_2 N + K_3 N^2 + . \cdots = \ln P \sum_{i=1}^{m} K_i N^{i=1} \tag{4}$$

Fitting was carried out using the least-squares method by varying the number of terms, until a suitable number of terms, m, described the isotherms adequately. Coefficients K_1, K_2, ... K_m are characteristic constants for a given gas–solid system and temperature. The Henry's constant for each gas, K_H, is the limiting value of N/P as $P \to 0$ and is given by eq 5.

$$K_H = \lim_{P\to 0}\left(\frac{N}{P}\right) \cong e^{K_1} \tag{5}$$

To calculate the standard deviations, all isotherms obtained experimentally for each component were fitted individually. The K_H values from all isotherms were averaged, and the average values were used to calculate selectivities by taking the ratios. Standard deviations for the ratios were calculated using rules for propagation of error.[89]

■ ASSOCIATED CONTENT

Supporting Information

The Supporting Information is available free of charge at https://pubs.acs.org/doi/10.1021/acs.chemmater.3c01717.

(Appendix I) Quantitative elemental analysis data for all C and EC aerogels of this study; (Appendix II) virial fitting of CO_2 isotherms at 273 K and 298; and (Appendix III) selectivity for CO_2 against other gases at 273 K (PDF)

■ AUTHOR INFORMATION

Corresponding Authors

Nicholas Leventis − *Department of Chemistry, Missouri S&T, Rolla, Missouri 65409, United States;* Present Address: Present address: Aspen Aerogels Inc., 30 Forbes Road, Bldg. B, Northborough, Massachusetts 01532, United States (N.L.); Email: nleventis@aerogel.com

Chariklia Sotiriou-Leventis − *Department of Chemistry, Missouri S&T, Rolla, Missouri 65409, United States;* orcid.org/0000-0003-3283-8257; Email: cslevent@mst.edu

Authors

Vaibhav A. Edlabadkar − *Department of Chemistry, Missouri S&T, Rolla, Missouri 65409, United States;* orcid.org/0000-0001-5763-7318

Rushi U. Soni − *Department of Chemistry, Missouri S&T, Rolla, Missouri 65409, United States;* orcid.org/0000-0002-1855-8905

A. B. M. Shaheen ud Doulah − *Department of Chemistry, Missouri S&T, Rolla, Missouri 65409, United States;* orcid.org/0000-0002-5413-0762

Stephen Y. Owusu − *Department of Chemistry, Missouri S&T, Rolla, Missouri 65409, United States;* orcid.org/0000-0002-5251-4287

Samuel Hackett − *Department of Chemistry, Missouri S&T, Rolla, Missouri 65409, United States*

Joshua M. Bartels − *Aspen Aerogels, Northborough, Massachusetts 01532, United States*

Complete contact information is available at: https://pubs.acs.org/10.1021/acs.chemmater.3c01717

Notes

The authors declare no competing financial interest.

https://doi.org/10.1021/acs.chemmater.3c01717
Chem. Mater. 2024, 36, 1172−1187

■ ACKNOWLEDGMENTS

We thank the NSF for financial support under award number CMMI-1530603 (subcontract to MS&T from Tufts University).

■ REFERENCES

(1) Atmospheric CH_4 Levels Graph https://www.methanelevels.org/ (6−23−2023)
(2) Earth's CO_2 Home Page www.co2.earth (6−23−2023)
(3) Masson-Delmotte, V.; Zhai, P.; Pörtner, H. O.; Roberts, D.; Skea, J.; Shukla, P. R.; Pirani, A.; Moufouma-Okia, W.; Péan, C.; Pidcock, R.; Connors, S., 2018. Global warming of 1.5 C. *An IPCC Special Report on the impacts of global warming of 1.5 oC 2018*, *1*, 43−50.
(4) Manabe, S. Role of Greenhouse Gases in Climate Change. *Tellus A* **2022**, *71*, 1620078.
(5) Kulkarni, S. J. Green House Gases − a Brief Review. *International Journal of Research and Review* **2017**, *4*, 18−21.
(6) The Causes of Climate Change https://climate.nasa.gov/causes/ (6−23−2023)
(7) Analysis: Coronavirus set to cause largest ever annual fall in CO_2 emissions https://www.carbonbrief.org/analysis-coronavirus-set-to-cause-largest-ever-annual-fall-in-co2-emissions (6−23−2023)
(8) Haszeldine, R. S. Carbon Capture and Storage: How Green Can Black Be? *Science* **2009**, *325*, 1647−1652.
(9) Smit, B.; Reimer, J.; Oldenburg, C.; Bourg, I. *Introduction to Carbon Capture and Sequestration: The Berkeley Lectures on Energy*; *Vol. 1*, Imperial College Press: London, 2014, 141−162.
(10) Meng, F.; Meng, Y.; Ju, T.; Han, S.; Lin, L.; Jiang, J. Research Progress of Aqueous Amine Solution for CO_2 Capture: A Review. *Renewable and Sustainable Energy Reviews* **2022**, *168*, No. 112902.
(11) Chen, G.; Wang, T.; Zhang, G.; Liu, G.; Jin, W. Membrane Materials Targeting Carbon Capture and Utilization. *Adv. Membr.* **2022**, *9*, No. 100025.
(12) Pardakhti, M.; Jafari, T.; Tobin, Z.; Dutta, B.; Moharreri, E.; Shemshaki, N. S.; Suib, S.; Srivastava, R. Trends in Solid Adsorbent Materials Development for CO_2 Capture. *ACS Appl. Mater. Interfaces* **2019**, *38*, 34533−34559.
(13) Mahajan, S.; Lahtinen, M. Recent Progress in Metal-organic Frameworks (MOFs) for CO_2 Capture at Different Pressures. *Journal of Environmental Chemical Engineering* **2022**, *10*, No. 108930.
(14) Piscopo, C. G.; Loebbecke, S. Strategies to Enhance Carbon Dioxide Capture in Metal-Organic Frameworks. *ChemPlusChem.* **2020**, *85*, 538−547.
(15) Zhou, H.; Rayer, C.; Antonangelo, A. R.; Hawkins, N.; Carta, M. Adjustable Functionalization of Hyper-Cross-Linked Polymers of Intrinsic microporosity for Enhanced CO_2 Adsorption and Selectivity over N_2 and CH_4. *ACS Appl. Mater. Interfaces* **2022**, *18*, 20997−21006.
(16) Lee, J. S. M.; Cooper, A. I. Advances in Conjugated Microporous Polymers. *Chem. Rev.* **2020**, *4*, 2171−2214.
(17) He, G.; Huang, S.; Villalobos, L. F.; Vahdat, M. T.; Guiver, M. D.; Zhao, J.; Lee, W.; Mensi, M.; Agrawal, K. V. Synergistic CO_2-Sieving from Polymer with Intrinsic microporosity Masking Nanoporous Single-Layer Graphene. *Adv. Funct. Mater.* **2020**, *30*, 2003979.
(18) Yuan, Y.; Zhu, G. Porous Aromatic Frameworks as a Platform for Multifunctional Applications. *ACS Cent. Sci.* **2019**, *3*, 409−418.
(19) Abdelnaby, M. M.; Qasem, N. A. A.; Al-Maythalony, B. A.; Cordova, K. E.; Al Hamouz, O. C. S. A Microporous Organic Copolymer for Selective CO_2 Capture under Humid Conditions. *ACS Sustainable Chem. Eng.* **2019**, *16*, 13941−13948.
(20) Kundu, N.; Sarkar, S. Porous Organic Frameworks for Carbon dioxide Capture and Storage. *J. Environ. Chem. Eng.* **2021**, *9*, No. 105090.
(21) Klumpen, C.; Radakovitsch, F.; Jess, A.; Senker, J. BILP-19- An Ultramicroporous Organic Network with Exceptional Carbon Dioxide Uptake. *Molecules* **2017**, *22*, 1343.
(22) Guo, P.; Dutta, D.; Wong-Foy, G. A.; Gidley, W. D.; Matzger, J. A. Water Sensitivity in Zn_4O-based MOFs is Structure and History Dependent. *J. Am. Chem. Soc.* **2015**, *137*, 2651−2657.
(23) Schoenecker, P. M.; Carson, G. C.; Jasuja, H.; Flemming, J. J. C.; Walton, K. S. Effect of Water Adsorption on Retention of Structure and Surface Area of Metal−Organic Frameworks. *Ind. Eng. Chem. Res.* **2012**, *51*, 6513−6519.
(24) Davis, M. E. Ordered Porous Materials for Emerging Applications. *Nature* **2002**, *417*, 813−821.
(25) McKeown, N. B.; Budd, P. M. Polymers of Intrinsic microporosity (PIMs): Organic Materials for Membrane Separations, Heterogeneous Catalysis and Hydrogen Storage. *Chem. Soc. Rev.* **2006**, *35*, 675−683.
(26) McKeown, N. B.; Budd, P. M.; Msayib, K. J.; Ghanem, B. S.; Kingston, H. J.; Tattershall, C. E.; Makhseed, S.; Reynolds, K. J.; Fritsch, D. Polymers of Intrinsic microporosity (PIMs): Bridging the Void between Microporous and Polymeric Materials. *Chem. - Eur. J.* **2005**, *11*, 2610−2620.
(27) Saeed, A. M.; Wisner, C. A.; Donthula, S.; Majedi Far, H.; Sotiriou-Leventis, C.; Leventis, N. Reuseable Monolithic Nanoporous Graphite-Supported Nanocatalysts (Fe, Au, Pt, Pd, Ni, and Rh) from Pyrolysis and Galvanic Transmetalation of Ferrocene-Based Polyamide aerogels. *Chem. Mater.* **2016**, *28*, 4867−4877.
(28) Tomasic, V.; Jovic, F. State-of-the-art in the Monolithic Catalysts/Reactors. *Appl. Catal., A* **2006**, *311*, 112−121.
(29) Twigg, M. V. Catalytic Control of Emissions from Cars. *Catal. Today* **2011**, *163*, 33−41.
(30) Leventis, N.; Elder, I. A.; Rolison, D. R.; Anderson, M. L.; Merzbacher, C. I. Durable Modification of Silica Aerogel Monoliths with Fluorescent 2,7-Diazapyrenium Moieties. Sensing Oxygen near The Speed of Open-Air Diffusion. *Chem. Mater.* **1999**, *11*, 2837−2845.
(31) Soni, R. U.; Edlabadkar, V. A.; Greenan, D.; Rewatkar, P. M.; Leventis, N.; Sotiriou-Leventis, C. Preparation of Carbon aerogels from Polymer-Cross-Linked Xerogel Powders without Supercritical Fluid Drying and Their Application in Highly Selective CO_2 Adsorption. *Chem. Mater.* **2022**, *34*, 4828−4847.
(32) Saeed, A. M.; Rewatkar, P. M.; Majedi Far, H.; Taghvaee, T.; Donthula, S.; Mandal, C.; Sotiriou-Leventis, C.; Leventis, N. Selective CO_2 Sequestration with Monolithic Bimodal Micro/Macroporous Carbon aerogels Derived from Stepwise pyrolytic Decomposition of Polyamide-Polyimide-Polyurea Random Copolymers. *ACS Appl. Mater. Interfaces* **2017**, *9*, 13520−13536.
(33) Far, H. M.; Donthula, S.; Taghvaee, T.; Saeed, A. M.; Garr, Z.; Sotiriou-Leventis, C.; Leventis, N. Air-oxidation of Phenolic Resin aerogels: Backbone Reorganization, Formation of Ring-fused Pyrylium Cations, and the Effect on Microporous Carbons with Enhanced Surface Areas. *RSC Adv.* **2017**, *7*, 51104−51120.
(34) Mahadik-Khanolkar, S.; Donthula, S.; Sotiriou-Leventis, C.; Leventis, N. 1. High-Yield Room-Temperature Acid-Catalyzed Synthesis of Robust Monoliths, Oxidative Aromatization, and Conversion to Microporous Carbons. *Chem. Mater.* **2014**, *26*, 1303−1317.
(35) Soni, R. U.; Edlabadkar, V. A.; Rewatkar, P. M.; Doulah, S.; Leventis, N.; Sotiriou-Leventis, C. Low-Temperature Catalytic Synthesis of Graphite aerogels from Polyacrylonitrile-Crosslinked Iron Oxide and Cobalt Oxide Xerogel Powders. *Carbon* **2022**, *193*, 107−127.
(36) Chidambareswarapattar, C.; Xu, L.; Sotiriou-Leventis, C.; Leventis, N. Robust Monolithic multiscale Nanoporous polyimides and Conversion to Isomorphic Carbons. *RSC Adv.* **2013**, *3*, 26459.
(37) Rhine, W.; Wang, J.; Begag, R. Polyimide aerogels, Carbon aerogels, and Metal Carbide aerogels and Methods of Making Same. U.S. Patent No. 7,074,880 B2 (07−11−2006).
(38) Chidambareswarapattar, C.; McCarver, P. M.; Luo, H.; Lu, H.; Sotiriou-Leventis, C.; Leventis, N. Fractal multiscale Nanoporous Polyurethanes: Flexible to Extremely Rigid aerogels from Multifunctional Small Molecules. *Chem. Mater.* **2013**, *25*, 3205−3224.

https://doi.org/10.1021/acs.chemmater.3c01717
Chem. Mater. 2024, 36, 1172−1187

(39) Leventis, N.; Sotiriou-Leventis, C.; Saeed, A. M.; Donthula, S.; Majedi Far, H.; Rewatkar, P. M.; Kaiser, H.; Robertson, J. D.; Lu, H.; Churu, G. Nanoporous Polyurea from a Triisocyanate and Boric Acid: A Paradigm of a General Reaction Pathway for Isocyanates and Mineral Acids. *Chem. Mater.* **2016**, *2016* (28), 67−78.
(40) Leventis, N.; Sotiriou-Leventis, C.; Chandrasekaran, N.; Mulik, S.; Larimore, Z. J.; Lu, H.; Churu, G.; Mang, J. T. Multifunctional Polyurea aerogels from Isocyanates and Water. A Structure−property Case Study. *Chem. Mater.* **2010**, *22*, 6692−6710.
(41) Pekala, R. W.; Alviso, C. T.; Kong, F. M.; Hulsey, S. S. aerogels Derived from Multifunctional Organic Monomers. *J. Non-Cryst. Solids* **1992**, *145*, 90−98.
(42) Al-Muhtaseb, S. A.; Ritter, J. A. Preparation and Properties of Resorcinol−Formaldehyde Organic and Carbon Gels. *Adv. Mater.* **2003**, *15*, 101−114.
(43) Leventis, N.; Mulik, N. S.; Sotiriou-Leventis, C. Macroporous Electrically Conducting Carbon Networks by Pyrolysis of Isocyanate Cross-linked Resorcinol-formaldehyde aerogels. *Chem. Mater.* **2008**, *20*, 6985−6997.
(44) Malakooti, S.; Qin, G.; Mandal, C.; Soni, R.; Taghvaee, T.; Ren, Y.; Chen, H.; Tsao, N.; Shiao, J.; Kulkarni, S. S.; Sotiriou-Leventis, C.; Leventis, N.; Lu, H. Low-Cost, Ambient-Dried, Superhydrophobic, High Strength, Thermally Insulating, and Thermally Resilient Polybenzoxazine aerogels. *ACS Appl. Polym. Mater.* **2019**, *1*, 2322−2333.
(45) Edlabadkar, V. A.; Gorla, S.; Soni, R. U.; Doulah, A. S. U.; Gloriod, J.; Hackett, S.; Leventis, N.; Sotiriou-Leventis, C. Polybenzodiazine aerogels: All-Nitrogen Analogues of Polybenzoxazines - Synthesis, Characterization, and High-Yield Conversion to Nanoporous Carbons. *Chem. Mater.* **2023**, *35*, 432−446.
(46) Sevilla, M.; Valle-Vigón, P.; Fuertes, A. N-Doped Polypyrrole-Based Porous Carbons for CO_2 Capture. *Adv. Funct. Mater.* **2011**, *21*, 2781−2787.
(47) Dawson, R.; Cooper, A.; Adams, D. Chemical Tuning of CO_2 sorption in Robust Nanoporous Organic Polymers. *Polym. Int.* **2013**, *62*, 345−352.
(48) Majedi Far, H.; Rewatkar, P. M.; Donthula, S.; Taghvaee, T.; Saeed, A. M.; Sotiriou-Leventis, C.; Leventis, N. Exceptionally High CO_2 Adsorption at 273 K by Microporous Carbons from Phenolic aerogels: The Role of Heteroatoms in Comparison with Carbons from Polybenzoxazine and Other Organic aerogels. *Macromol. Chem. Phys.* **2019**, *220*, 1800333.
(49) Rahaman, M. S. A.; Ismail, A. F.; Mustafa, A. A Review of Heat Treatment on Polyacrylonitrile Fiber. *Polym. Degrad. Stab.* **2007**, *92*, 1421−1432.
(50) Usami, T.; Itoh, T.; Ohtani, H.; Tsuge, S. Structural Study of Polyacrylonitrile Fibers during Oxidative Thermal Degradation by Pyrolysis-Gas Chromatography, Solid-State Carbon-13 NMR, and Fourier-Transform Infrared Spectroscopy. *Macromolecules* **1990**, *23*, 2460−2465.
(51) Harkins, W. D.; Jura, G. Surfaces of Solids. XIII. A Vapor Adsorption Method for the Determination of the Area of a Solid without the Assumption of a Molecular Area, and the Areas Occupied by Nitrogen and Other Molecules on the Surface of a Solid. *J. Am. Chem. Soc.* **1944**, *66*, 1362−1373.
(52) Dubinin, M. M. Fundamentals of the Theory of Adsorption in Micropores of Carbon Adsorbents: Characteristics of their Adsorption Properties and Microporous Structures. *Carbon* **1989**, *27*, 457−467.
(53) Horvath, G.; Kawazoe, K. Method for the Calculation of Effective Pore Size Distribution in Molecular Sieve Carbon. *J. Chem. Eng. Jpn.* **1983**, *16*, 470−475.
(54) Cazorla-Amorós, D.; Alcañiz-Monge, J.; de la Casa-Lillo, M. A.; Linares-Solano, A. CO_2 as an Adsorptive to Characterize Carbon Molecular Sieves and Activated Carbons. *Langmuir* **1998**, *16*, 4589−4596.
(55) Webb, P. A.; Orr, C. *Analytical Methods in Fine Particle Technology*; Micromeritics Instrument Corporation: Norcross, GA, 1997; pp 81−87.
(56) Saha, B. B.; Jribi, S.; Koyama, I.; El-Sharkawy, I. Carbon Dioxide Adsorption Isotherms on Activated Carbons. *J. Chem. Eng. Data* **2011**, *56*, 1974−1981.
(57) Landers, J.; Gor, G. Y.; Neimark, A. V. Density Functional Theory Methods for Characterization of Porous Materials. *Colloids Surf. A* **2013**, *437*, 3−32.
(58) Figueiredo, J. L.; Pereira, M. F. R. The Role of Surface Chemistry in Catalysis with Carbons. *Catal. Today* **2010**, *150*, 2−7.
(59) Wickramaratne, N. P.; Jaroniec, M. Importance of Small Micropores in CO_2 Capture by Phenolic Resin-Based Activated Carbon Spheres. *J. Mater. Chem. A* **2013**, *1*, 112−116.
(60) Adeniran, B.; Mokaya, R. Low Temperature Synthesized Carbon Nanotube Superstructures with Superior CO_2 and Hydrogen Storage Capacity. *J. Mater. Chem. A* **2015**, *3*, 5148−5161.
(61) Cazorla-Amorós, D.; Alcañiz-Monge, J.; Linares-Solano, A. Characterization of Activated Carbon Fibers by CO_2 Adsorption. *Langmuir* **1996**, *12*, 2820−2824.
(62) Smit, B.; Reimer, J. R.; Oldenburg, C. M.; Bourg, I. C. Introduction to Carbon Capture and Sequestration: The Berkeley Lectures on Energy. *Imperial College Press: London* **2014**, *1*, 281−354.
(63) Myers, A. L. Characterization of Nanopores by Standard Enthalpy and Entropy of Adsorption of Probe Molecules. *Colloids Surf., A* **2004**, *241*, 9−14.
(64) Song, X.; Wang, L.; Ma, X.; Zeng, Y. Adsorption Equilibrium and Thermodynamics of CO_2 and CH_4 on Carbon Molecular Sieves. *Appl. Sur. Sci.* **2017**, *396*, 870−878.
(65) Lin, K.; Zhao, Y. Entropy and Enthalpy Changes during Adsorption and Displacement of Shale Gas. *Energy* **2021**, *221*, No. 119854.
(66) Nuhnen, A.; Janiak, C. A Practical Guide to Calculate the Isosteric Heat/Enthalpy of Adsorption *via* Adsorption Isotherms in Metal-Organic Frameworks. *MOFs. Dalton Trans.* **2020**, *49*, 10295−10307.
(67) Teo, H. W. B.; Chakraborty, A.; Kitagawa, Y.; Kayal, S. Experimental study of isotherms and kinetics for adsorption of water on Aluminium Fumarate. *Int. J. Heat Mass Transfer* **2017**, *114*, 621−627.
(68) Beckner, M.; Dailly, A. Adsorption Enthalpy Calculations of Hydrogen Adsorption at Ambient Temperature and Pressures Exceeding 300 bar. *Am. J. Anal. Chem.* **2013**, *4*, 8−16.
(69) Patel, H. A.; Je, S. H.; Park, J.; Jung, Y.; Coskun, A.; Yavuz, C. T. Directing the Structural Features of N_2-Phobic Nanoporous Covalent Organic Polymers for CO_2 Capture and Separation. *Chem. - Eur. J.* **2014**, *20*, 772−780.
(70) Donaldson, T. L.; Nguyen, Y. N. Carbon Dioxide Reaction Kinetics and Transport in Aqueous Amine Membranes. *Ind. Eng. Chem. Fundam.* **1980**, *19*, 260−266.
(71) Richner, G.; Puxty, G. Assessing the Chemical Speciation during CO_2 Absorption by Aqueous Amines Using in Situ FTIR. *Ind. Eng. Chem. Res.* **2012**, *51*, 14317−14324.
(72) Bollini, P.; Didas, S. A.; Jones, C. W. Amine-Oxide Hybrid Materials for Acid Gas Separations. *J. Mater. Chem.* **2011**, *21*, 15100−15120.
(73) Didas, S. A.; Sakwa-Novak, M. A.; Foo, G. S.; Sievers, C.; Jones, C. W. Effect of Amine Surface Coverage on the C-Adsorption of CO_2 and Water: Spectral Deconvolution of Adsorbed Species. *J. Phys. Chem. Lett.* **2014**, *5*, 4194−4200.
(74) Zhu, Z.; Parker, S. T.; Forse, A. C.; Lee, J.-H.; Siegelman, R. L.; Milner, P. J.; Tsai, H.; Ye, M.; Xiong, S.; Paley, M. V.; Uliana, A. A.; Oktawiec, J.; Dinakar, B.; Didas, S. A.; Meihaus, K. R.; Reimer, J. A.; Neaton, J. B.; Long, J. R. Cooperative Carbon Dioxide Capture in Diamine-Appended Magnesium-Olsalazine Frameworks. *J. Am. Chem. Soc.* **2023**, *145*, 17151−17163.
(75) *March's Advanced Organic Chemistry* (Eds: M. B. Smith, J. March); John Wiley & Sons, Inc.: Hoboken, NJ, 2007; pp 3−31.
(76) Siegelman, R. L.; Milner, P. J.; Forse, A. C.; Lee, J.-H.; Colwell, K. A.; Neaton, J. B.; Reimer, J. A.; Weston, S. C.; Long, J. R. Water Enables Efficient CO_2 Capture from Natural Gas Flue Emissions in an

https://doi.org/10.1021/acs.chemmater.3c01717
Chem. Mater. 2024, 36, 1172−1187

Oxidation-Resistant Diamine-Appended Metal-Organic Framework. *J. Am. Chem. Soc.* **2019**, *141*, 13171−13186.
(77) Chen, C. H.; Shimon, D.; Lee, J. J.; Didas, S. A.; Mehta, A. K.; Sievers, C.; Jones, C. W.; Hayes, S. E. Spectroscopic Characterization of Adsorbed $^{13}CO_2$ on 3-Aminopropylsilyl-Modified SBA15 Mesoporous Silica. *Environ. Sci. Technol.* **2017**, *51*, 6553−6559.
(78) Freitas, J. C. C.; Cipriano, D. F.; Zucolotto, C. G.; Cunha, A. G.; Emmerich, F. G. Solid-State ^{13}C NMR Spectroscopy Applied to the Study of Carbon Blacks and Carbon Deposits Obtained by Plasma Pyrolysis of Natural Gas. *J. Spectrosc.* **2016**, 1543273.
(79) Jeong, K.; Arami-Niya, A.; Yang, X.; Xiao, G.; Lipinski, G.; Aman, Z. M.; May, E. F.; Richter, M.; Stanwix, P. L. Direct Characterization of Gas Adsorption and Phase Transition of a Metal Organic Framework Using In-situ Raman Spectroscopy. *Chem. Eng. J.* **2023**, *473*, No. 145240.
(80) Lipinski, G.; Jeong, K.; Moritz, K.; Petermann, M.; May, E. F.; Stanwix, P. L.; Richter, M. Application of Raman Spectroscopy for sorption Analysis of Functionalized Porous Materials. *Adv. Sci.* **2022**, *9*, 2105477.
(81) Lipinski, G.; Holzammer, C.; Petermann, M.; Richter, M. Measurement of sorption Phenomena Near Dew Points of Fluid Mixtures: Concept for the Combination of Gravimetric sorption Analysis and Raman Spectroscopy. *Meas. Sci. Technol.* **2018**, *29*, 105501.
(82) Nath, K.; Ahmed, A.; Siegel, D. J.; Matzger, A. J. Microscale Determination of Binary Gas Adsorption Isotherms in MOFs. *J. Am. Chem. Soc.* **2022**, *144*, 20939−20946.
(83) Yoon, D.; Cheong, H. Raman Spectroscopy for Characterization of Graphene, in *Raman Spectroscopy for Nanomaterials Characterization*. Ed.: Kumar, C. S. S. R., Springer: Berlin, Germany, 2012; pp 191−214.
(84) *Laser Speckle and Related Phenomena*. Vol. *9*. Dainty, J. C., Ed. Springer Science & Business Media, 2013.
(85) Dawson, R.; Cooper, A. I.; Adams, D. J. Chemical Functionalization Strategies for Carbon Dioxide Capture in Microporous Organic Polymers. *Polym. Int.* **2013**, *62*, 345−352.
(86) Dubskikh, V. A.; Kovalenko, K. A.; Nizovtsev, A. S.; Lysova, A. A.; Samsonenko, D. G.; Dybtsev, D. N.; Fedin, V. P. Enhanced Adsorption Selectivity of Carbon Dioxide and Ethane on Porous Metal−Organic Framework Functionalized by a Sulfur-Rich Heterocycle. *Nanomaterials* **2022**, *12*, 4281.
(87) Sing, K. S. W.; Rouquerol, F.; Rouquerol, J. Adsorption by Powders and Porous Solids (Eds: Rouquerol, F.; Rouquerol, J.; Sing, K. S. W.; Llewellyn, P.; Maurin, G.), Academic Press: Oxford, 2014; pp 159−163.
(88) Rallapalli, P.; Prasanth, K. P.; Patil, D.; Somani, R. S.; Jasra, R. V.; Bajaj, H. C. sorption Studies of CO_2, CH_4, N_2, CO, O_2 and Ar on Nanoporous Aluminum Terephthalate [MIL-53(Al)]. *J. Porous Mater.* **2011**, *18*, 205−210.
(89) https://www.eoas.ubc.ca/courses/eosc252/error-propagation-calculator-fj.htm. (6−23−2023)

https://doi.org/10.1021/acs.chemmater.3c01717
Chem. Mater. 2024, 36, 1172−1187